

COBALT-ANCHORED VANADIUM CARBIDE MXENE NANOCOMPOSITE FOR SUPERCAPACITOR AND WATER SPLITTING APPLICATIONS



Ebrima Ceesay

[MS Physics]

Registration number: 359401

Session: 2020-2022

Supervisor: Prof. Syed Rizwan Hussain

Department of Physics, School of Natural Sciences


National University of Sciences and Technology

Islamabad, Pakistan

September 2022

National University of Sciences & Technology**MS THESIS WORK**

We hereby recommend that the dissertation prepared under our supervision by: **Ebrima Ceesay**, Regn No. **00000359401** Titled: "**Cobalt-Anchored Vanadium Carbide MXene Nanocomposite for Supercapacitor and Water Splitting Applications**" accepted in partial fulfillment of the requirements for the award of **MS** degree.

Examination Committee Members1. Name: DR. FAHEEM AMINSignature: 2. Name: DR. GHULAM ALISignature: Supervisor's Name: PROF. SYED RIZWAN HUSSAINSignature: 
Head of Department10-10-2022
Date**COUNTERSIGNED**Date: 10.10.2022
Dean/Principal

DEDICATION

To my mother Nyaranding Jammeh and father Sainey Ceesay, who instilled and nurtured in me the desired to excel.

May Allah forgive, bless, and grant them Jannatul-Firdaus.

My wife (Nyimasatou)

My children (Jariatou, Fatou , Muhammad Sarjo and Halima)

We All did it!

ACKNOWLEDGEMENT

In the Name of Allah, the Most Compassionate, the Most Merciful.

Alhamdulillah Rabil Alameen Alhamdulillah Rabil Alameen Alhamdulillah Rabil Alameen

I would like to express my deepest gratitude and thanks to my supervisor Prof. Dr. Syed Rizwan Hussain, for his guidance, support, and the conducive environment he created throughout the course of my research. I am indeed grateful.

Sincere appreciation to my GEC members Dr. Faheem Amin and Dr. Ghulam Ali for their contribution during this research.

Appreciation and thanks to staff and faculty of School of Natural Sciences especially the Physics department.

To all my research group members in 2D nanomaterials especially my seniors.

I did not walk this journey alone, thanks to your support and kindness, I made it this far.

ABSTRACT

Electrochemical Capacitors and Hydrogen production through water splitting into constituent H_2 and O_2 is a captivating way out for long-lasting energy storage. Developing an efficient and versatile nanocomposite from earth-abundant elements that is stable and active for storing energy and conversion is pivotal with regards to cost and convenience to simplify the overall system design. This thesis presented a simple, cheap and one step synthesis of Cobalt-doped Vanadium Carbide MXene ($Co@V_2CT_x$) nanocomposite through co-precipitation method, to be utilized as an effective, durable, and stable electrode for supercapacitor and as an electrocatalyst for water electrolysis. In 1M KOH, the $Co@V_2CT_x$ nanocomposite supported on a nickel foam produced at $2mVs^{-1}$, a capacitance of $1259Fg^{-1}$. Also, its specific charge capacity is $82.2 Ahg^{-1}$, energy, and power density of $26.7Whkg^{-1}$ and $325Wkg^{-1}$ respectively at $1Ag^{-1}$ current density. In addition, the $Co@V_2CT_x$ nanocomposite shows excellent HER and OER catalytic activity exhibiting a minimal overpotential of 103mV and 170mV respectively at $10mAcm^{-2}$ and Tafel slope of $83mVdec^{-1}$ for HER and $145mVdec^{-1}$ for OER, which is comparable to commercial Platinum catalyst. This excellent performance of $Co@V_2CT_x$ nanocomposite may be due to the synergistic effects produced when Cobalt is intercalated into Vanadium Carbide MXene. This thesis features an easy, cheap, and effective method to synthesis MXene-based nanocomposite for application for energy storage and conversion.

Key words: Supercapacitor, Synergetic, Hydrogen Evolution Reaction, Overpotential, Specific capacitance.

TABLE OF CONTENT

CHAPTER 1 INTRODUCTION	8
1.1. Background and Motivation	8
1.2. Supercapacitors (SCs).....	8
1.3. Electrocatalytic water splitting	9
1.3.1. Choice of electrolyte	10
1.4. Why MXene based nanocomposites	11
1.5. Research Objectives	13
CHAPTER 2 LITERATURE REVIEW	14
2.1. Synthesis of MXenes-based composites.....	14
2.2. Vanadium Carbides and its composites for supercapacitor	15
2.3. Vanadium Carbides and its composites for electrochemical water splitting	16
2.4. Cobalt based composites for Electrochemical water splitting.....	16
CHAPTER 3 EXPERIMENTATION	17
3.1. Synthesis of MXene.....	17
3.2. Common methods through which MXene composites are synthesized	17
3.2.1. Solvothermal and Hydrothermal synthesis.....	17
3.2.2. Co-precipitation method.....	17
3.2.3. Deposition methods.....	18
3.2.4. Solution processing.....	18
3.3. Synthesis and Characterization.....	19
3.3.1. Synthesis of multilayer V ₂ CT _x MXene.....	19
3.3.2. Synthesis of Cobalt nitrate/Vanadium carbide nanocomposites	19
3.3.3. Electrode fabrication.....	20
3.4. Characterizations tools	20
3.4.1. X-ray Diffraction (XRD)	21
3.4.2. Scanning Electron Microscopy (SEM) and Energy Dispersive X-ray (EDX).....	22
3.4.3. Raman Spectroscopy (Raman)	23
3.4.4. Fourier Transform Infrared Spectroscopy-FTIR	24
3.4.5. Thermogravimetric Analysis/Differential Scanning Calorimetry (DSC /TGA)	25
3.5. Electrochemical Measurements	26
CHAPTER 4 RESULTS AND DISCUSSION	28
4.1. Results from Characterization tools.....	28
4.1.1. X-Ray Diffraction	28
4.1.2. Scanning Electron Microscopy (SEM) and Energy Dispersive X-ray (EDX).....	29

4.1.3. Raman Spectroscopy.....	31
4.1.4. Fourier Transform Infrared Spectroscopy.....	32
4.1.5. Thermogravimetric Analysis/Differential Scanning Calorimetry (TGA/DSC)	33
4.2. Electrochemical characterization and measurements	35
4.2.1. Cyclic voltammetry.....	35
4.2.2. Galvanostatic Charge Discharge (GCD)	38
4.2.3. Linear Sweep voltammetry(LSV).....	40
4.2.3.1. Hydrogen Evolution Reaction (HER)	40
4.2.3.2. Oxygen Evolution Reaction(OER).....	43
4.2.4. Impedance Spectroscopy (EIS).....	46
CHAPTER 5 CONCLUSION AND WAYFORWARD	49
LIST OF PUBLICATION/ SUBMISSION	50
REFERENCES.....	51

LIST OF FIGURES

Figure 1: Types of electrochemical capacitors a) EDLC b) Pseudocapacitor and c) Hybrid Supercapacitor. Reproduced with permission from reference [7].	9
Figure 2: Illustration of OER and HER cell design and activity . Adapted with permission from reference [9].	10
Figure 3: Illustration showing some applications of MXene. Adapted with permission from reference [14].	12
Figure 4: Elements on the periodic table that constitute M, X, and T in MXene.	13
Figure 5: Schematic illustration of V ₂ CT _x synthesis and anchoring of Co on V ₂ CT _x sheets.	20
Figure 6: Illustration of diffraction rays and Bragg's law [69].	22
Figure 7: Parts of the SEM showing internal structure [69].	23
Figure 8: Schematics Illustration of the working principle of Raman [70].	24
Figure 9: Schematic showing the working principle of FTIR [76].	25
Figure 10: Schematic diagram showing parts of the thermogravimetric analysis instrument [71].	26
Figure 11: XRD of etched V ₂ CT _x , and various Co@ V ₂ CT _x composites.	28
Figure 12: micrographs from SEM of a) V ₂ AIC b) V ₂ CT _x MXene, and c) Co@V ₂ CT _x d) element mapping of Co@V ₂ CT _x nanocomposites showing the presence and distribution of V,C, Co, O, Al, and F e) EDX show the percentage weight of elements in V ₂ CT _x MXene, and Co@V ₂ C.	30
Figure 13: Raman spectra for V ₂ AIC, V ₂ CT _x , Co and Co@V ₂ CT _x .	32
Figure 14: FTIR showing V ₂ CT _x and various samples of Co@V ₂ CT _x .	33
Figure 15: TGA/DSC plot for a) V ₂ CT _x and b) Co@V ₂ CT _x nanocomposite.	34
Figure 16: Voltammograms of V ₂ CT _x for different scan rates.	36
Figure 17: CV curves of Co@V ₂ CT _x (CoV1) at different scan rates.	37
Figure 18: Scan rate vs Specific capacitance of various samples.	38
Figure 19: GCD curves for Co@V ₂ CT _x (CoV1).	39
Figure 20: Cycling stability of Co@V ₂ CT _x (CoV1).	40
Figure 21: a) HER polarization curves and b) Overpotential at 10mAcm ⁻² and 20mAcm ⁻² for CoV1, CoV2, CoV3, V ₂ CT _x , and Co.	41
Figure 22: Tafel slope for CoV1, CoV2, CoV3, V ₂ CT _x , and Co.	42
Figure 23: a) OER polarization and b) Overpotential at 10mAcm ⁻² and 20mAcm ⁻² for CoV1, CoV2, CoV3, V ₂ CT _x , and Co.	44
Figure 24: Tafel slopes representing CoV1, CoV2, CoV3, V ₂ CT _x , and Co.	45
Figure 25: Stability measurements of CoV1 for 14h.	46
Figure 26: Nyquist plot with fitting and equivalent circuit for V ₂ CT _x .	47
Figure 27: Nyquist plot with fitting and equivalent circuit for CoV1.	48

CHAPTER 1 | INTRODUCTION

1.1. Background and Motivation

As the global population is increasing, the demand for energy is as well increasing to meet the increasing population's consumption, and hence fossil fuels cannot meet such demands. This results in overprice and sometimes scarcity. Also, fossil fuels are non-renewable and environmentally hazardous.

Various findings have revealed that energy utilization positively influences economic prosperity [1]. Although utilization of energy stimulates economic development, it also hinders and cause adverse effect on the environment through pollution [2].

With these uncertainties, limitations and the environmental implications surrounding fossil fuels, batteries come into play, to address some of the challenges. However, batteries also have their limitations such as low power density, their waste is hazardous, and are expensive [3, 4].

A clean and reliable energy source is important for the environment and economic prosperity. There has been a surge in a new, alternative, and safer source of energy to meet the global demand. Researchers have been trying to develop high performing electrochemical capacitor alias supercapacitors and a way to harness hydrogen gas, a green, renewable, and environmentally friendly energy as a supplement and alternative to batteries and fossil fuel.

1.2. Supercapacitors (SCs)

An electrochemical capacitor alias supercapacitor is a superior kind of a typical capacitor that has elevated capacitance and minimal internal resistance that unfolds the room for large power density. Besides, the disparity in charge storage process of supercapacitor enlarges its energy density in comparison to a typical capacitor [5].

Depending on the way charges are stored, which is meticulously associated to the composition and the materials used, SCs are commonly categorized in three group namely electric double-layer capacitor-EDLC (figure 1a), Pseudocapacitor (figure 1c), and hybrid supercapacitor-HSC (figure 1c).

As a prospective energy storage device, electrochemical capacitors have been employed in several areas like automobile, energy acquisition and in power grid system as a result of its exceptional ability to have higher power density, lasting cycle life, operational within a varied

range of temperature amongst others. Supercapacitors can provide high power at a short period of time. As a result of its superior power density, fast charging, durability, and environmental friendliness in comparison to batteries, supercapacitors are theorized to be a potential substitute for batteries. Nevertheless, SCs are deficient in energy density in comparison to batteries [6]. Though, choice and composition of electrode material is of paramount importance, the SCs performance is also influenced by the electrolyte used. Therefore, it is crucial to study and select a befitting electrode and electrolyte to obtain a storage device with the desirable outcome [5].

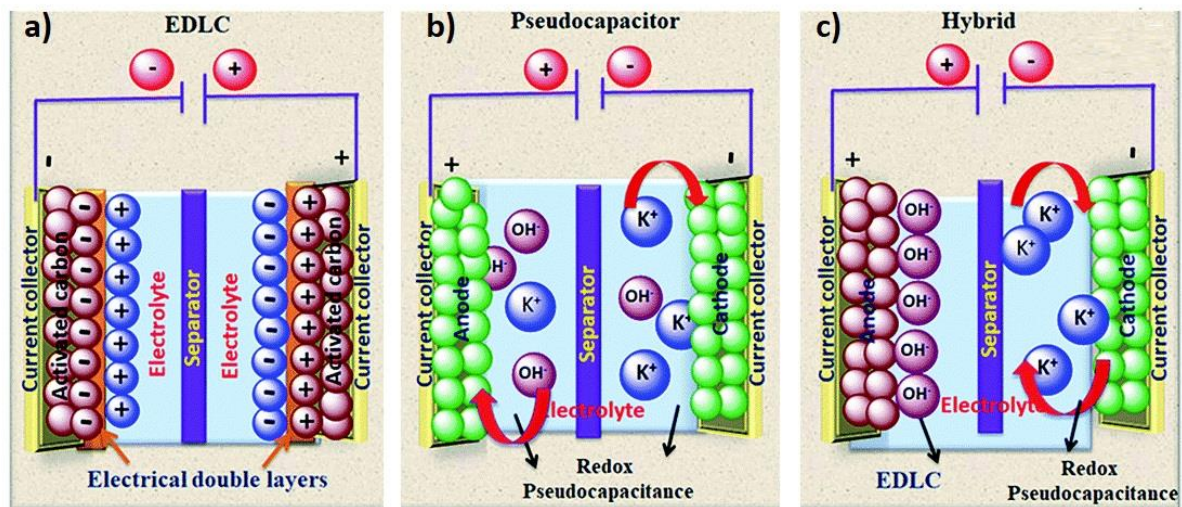


Figure 1: Types of electrochemical capacitors a) EDLC b) Pseudocapacitor and c) Hybrid Supercapacitor. Reproduced with permission from reference [7].

1.3. Electrocatalytic water splitting

A clean energy (hydrogen), that is renewable, can be obtained using a sophisticated technology like water electrolysis even at industrial scale [7].

The process through which water can be split to its constituent molecules of hydrogen and oxygen using energy is referred to as water electrolysis or water splitting. The whole process is geared towards renewable, clean, reliable, and sustainable energy, hence the energy required to do the electrolysis process should come from clean renewable energy sources like solar radiation, wind, hydro energy amongst others.

Through evolution of hydrogen (HER) at the cathode and evolution of oxygen (OER) at the anode, water molecules can be split into H_2 and O_2 (figure 2). HER and OER are called half reactions and their reaction parameters are studied closely to assess the whole splitting

process. HER is the mostly preferred to assess the performance of water splitting as it leads to the production of hydrogen. The overall reaction is summarized as:

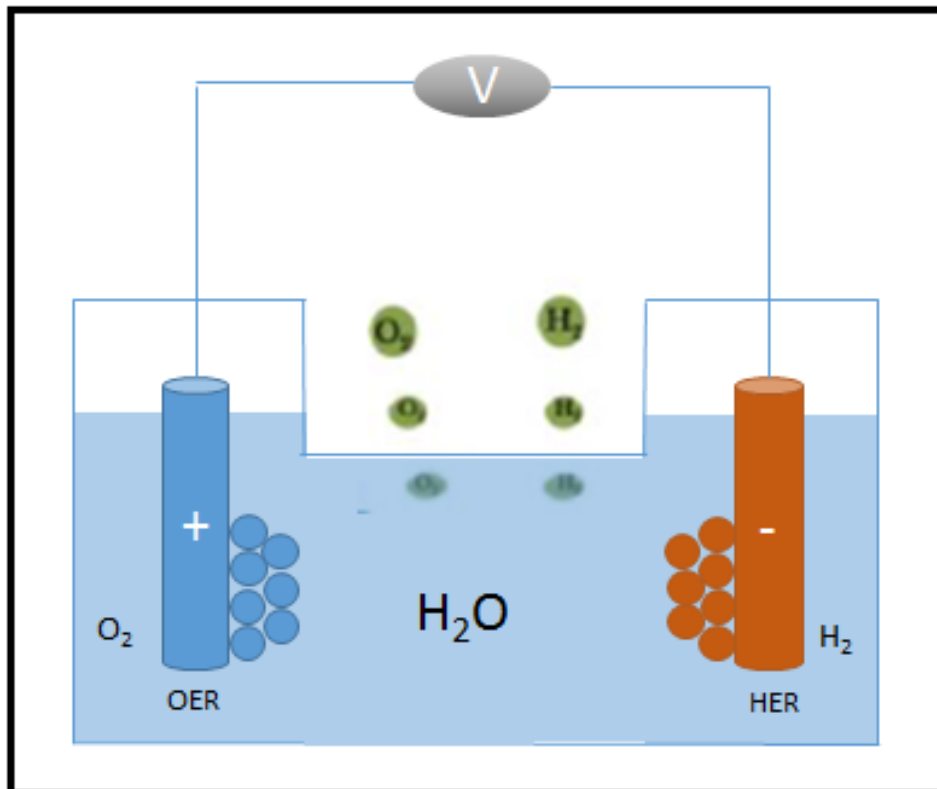
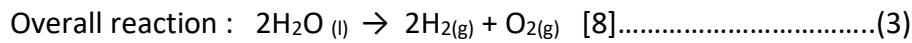
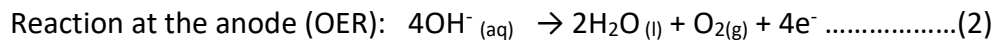
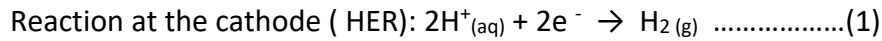


Figure 2: Illustration of OER and HER cell design and activity . Adapted with permission from reference [9]

1.3.1. Choice of electrolyte

Water electrolysis can either take place in acidic or alkaline media.

Acidic media:

- ❖ Has higher proton activity.
- ❖ Good for OER as it efficiently produces O₂ at a faster rate.
- ❖ But it limits catalyst to precious metals like Ru, Rh, Pt, Ag, Au and so on which are rare and expensive.

Alkaline media:

- ❖ Variety of catalysts like metal oxides and non-noble metals can be use.
- ❖ It is safer compared to acidic electrolytes.
- ❖ But its performance is 3 folds less than that of acidic electrolyte.

Due to sluggish kinetics and higher overpotential associated with OER, HER becomes the favorite in producing molecule hydrogen. To do this, energy and a catalyst is required to help the reaction process [9].

Noble metal such as platinum is excellent candidates for overall water splitting, producing exceptionally superior performance characteristics (Overpotential, Tafel slopes, charge transfer resistances and stability). However, such metals are expensive and thus limit their application to overall water splitting [10]. Progress has been made in the improvement of nanomaterial that are noble (corrosion and oxidation resistance) metals and other transition metals electrocatalysts for HER [10-12].

1.4. Why MXene based nanocomposites

Innovative nanomaterials coupled with sophisticated nanotechnology, continuously drive forward to a swift advancement of reliable and lasting energy production as well as storage means. A promising and emergent member of two-dimensional materials, MXene composed of transition-metal carbides, nitrides and carbonitrides. MXene has attracted growing interest and in-depth research due to their underlying properties and are widely use in numerous application (see figure 3).

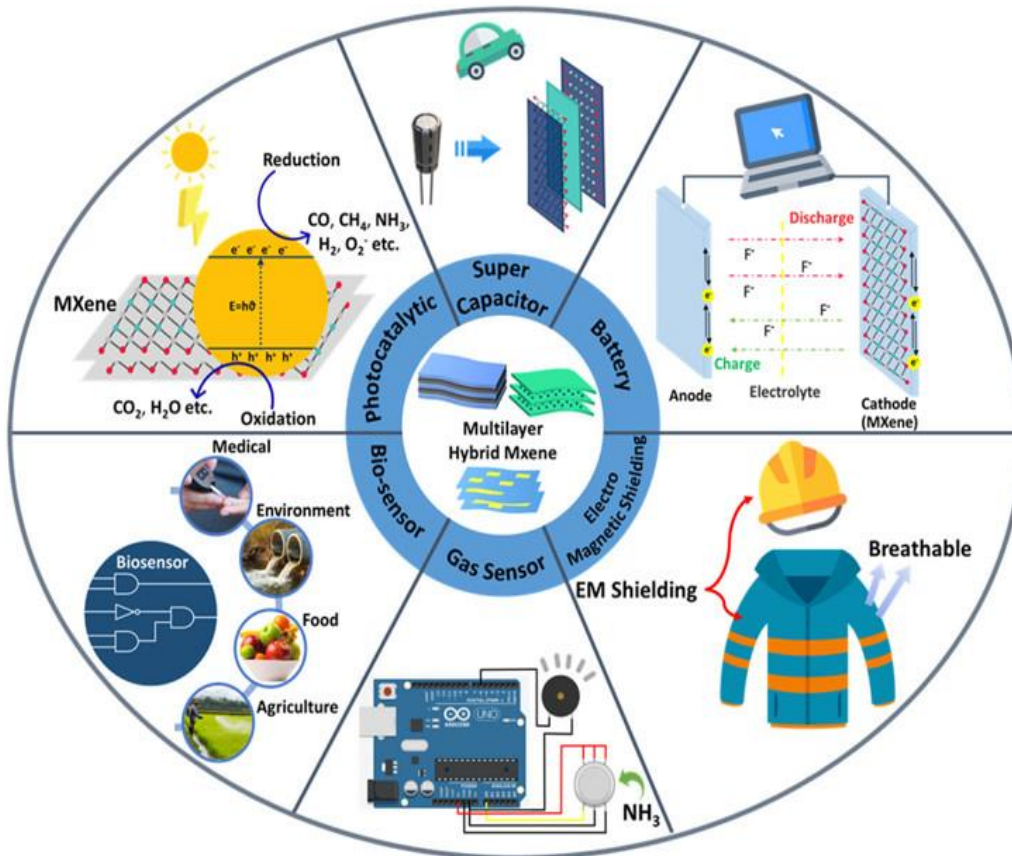
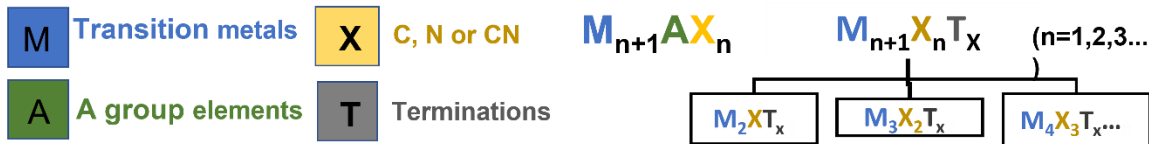


Figure 3: Illustration showing some applications of MXene. Adapted with permission from reference [14].

MXenes are two-dimensional layered and nanostructured materials which come from the parent MAX phase. They consist of metals in transition group (Hf, Cr, Mo, V, Ti, Nb), carbides, nitrides and/or Carbonitrides in form of $M_{n+1}X_nT_x$ ($n=1,2,3$), where M referred to metals in transition group, X can be a Carbon, Nitrides or carbonitrides and T_x denotes surface terminations (OH, O, or F) which results from synthesis of MXene from MAX phase as shown in figure 4. Some popular and most synthesized MXenes includes $Ti_3C_2T_x$, Ti_2CT_x , V_2CT_x and Nb_2CT_x . MXenes are strong, flexible, and highly conductive and hence these properties make them suitable to be utilized as an electrocatalyst in electrolysis of water and storage of energy application [13-15]. This new member of the two-dimensional nanomaterial is an exceptional candidate for energy storage owing to its large laminar-structured spacing, superior conductivity, rapid ion and molecule transport, hydrophilic nature, easily available structure, cycling and thermal stability, adjustable thickness, and a large surface to volume ratio [16, 17]. Considering the preceding information, MXenes appear to be the most auspicious electrode material for supercapacitors and water splitting.



The periodic table shows elements color-coded according to the legend: Transition metals (blue), A group elements (green), and Terminations (grey). The legend also defines the variables M, X, and T in the MXene formula.

Figure 4: Elements on the periodic table that constitute M, X, and T in MXene.

1.5. Research Objectives

The main objectives my thesis are

- ❖ to employ easy and cheap co-precipitation synthesis technique to synthesize nanostructured $Co@V_2CT_x$ that is stable, efficient, and cheap for an electrocatalysts and supercapacitor electrode.
- ❖ to study characteristics of Cobalt nitrate, V_2AlC , V_2CT_x , and $Co@V_2CT_x$ using Thermogravimetric Analysis and Differential Scanning Calorimetry (TGA/DSC), X-ray Diffraction (XRD), Fourier Transform Infrared Spectroscopy (FTIR), Raman Spectroscopy (Raman) and Scanning Electron Microscopy (SEM/EDX).
- ❖ to investigate the application of $Co@V_2CT_x$ in energy storage (supercapacitor) and water splitting.

CHAPTER 2 | LITERATURE REVIEW

MXenes have been used in many applications such as supercapacitors and batteries [18, 19], in electromagnetic interference shielding [20], sensors [21], water purifications membranes [22] and photothermal conversion [23] due to their outstanding performance and properties. Recently, electrochemical capacitors have attracted an enormous demand in massive manufacturing purposes in which they are utilized. As a result of their excellent performance in terms of rapid charging and discharging, durable cycling, and superior power density supercapacitors utilizations continue take momentum in automobiles and electronic gadgets. Moreover, electrochemical capacitors has the ability to function in wide ranges of temperature (40 to 150°C) and are small in size(compact), making them appropriate contender in advanced and sophisticated technologies in military, space, and telecommunication [24].

Similarly, researchers have been trying to develop a way to harness hydrogen gas, a green, renewable, and environmentally friendly energy as an alternative to batteries and fossil fuel. Through electrocatalysis water splitting, hydrogen can be harvested. Precious metal (resistant to corrosion and oxidation) like Ruthenium (Ru), Iridium (Ir) and Platinum (Pt), are efficient electrocatalyst plus they are one of the main parts to improve the efficiency of water decomposition process [25]. But due to their scarcity and excessive cost, it limits their application in commercial scale production.

This section presents the application of some recently reported MXene-based composites (focusing on Vanadium carbide MXene) in Supercapacitor and water splitting.

2.1. Synthesis of MXenes-based composites

One of the most efficient ways to enhance Mxene applications more specifically in supercapacitors and electrocatalytic water splitting is through the combination with other nanomaterials. Numerous methods have and can be used to carefully construct MXene composites and they includes Co-precipitation, Sol-gel, deposition methods, drop-casting and adsorption, and solution processing etc. [26]. These methods will be discussed in detail section 3.2 of chapter three.

2.2. Vanadium Carbides and its composites for supercapacitor

Kai C et al. in 2021 constructed a combination of V_2CT_x and $Ti_3C_2T_x$ MXene in the form of flexible films for superior performance of supercapacitor with varying percentage of $Ti_3C_2T_x$. Taking advantage of this well-designed nanocomposite, the V_2CT_x - $Ti_3C_2T_x$ MXene (flexible films) electrode establishes a good cycling stability even after 10,000 charging-discharging cycles, with no loss in capacitance. Moreover, at current density of $1 A g^{-1}$, it produced $365 F g^{-1}$, its energy and power density are $5.4 mWhg^{-1}$ at a power density of $357.8 mWg^{-1}$ respectively [27].

In 2022, Syedah AZ. et al. synthesized and investigated the performance of a supercapacitor electrode consisting of Vanadium carbide MXene and multi-wall nanotubes (carbon) denoted as $V_2CT_x/MWCNT$. At $2mVs^{-1}$, the electrode demonstrated an improved capacitance of $1842 F g^{-1}$, indicating the effect of the hybrid formed. Furthermore, the electrodes offered stability as it was able to retained 94% of its capacity after 10000 cycles [28].

In 2022, Pan J. et al. designed a structure through a heterojunction of V_2CT_x MXene/ NiV LDH resulting to good performance in a non-symmetric electrochemical capacitor. A capacitance of $1658.19 F g^{-1}$ at $1 A g^{-1}$ was realized and it was able to retained 80.95% of its capacity after 10,000 GCD cycles [29].

Mahjabeen F. et al. presented a detailed experimental and DFT (computation) to assess the performance of MnO_2 - V_2C nanocomposite utilized as electrode of supercapacitor. As compared to the V_2CT_x ($196.5 F/g$), it produced a higher capacitance of $551.8 Fg^{-1}$ and retained 95% of its capacity after 5000 cycles [30].

In their work, **Yuming Z. et al.** presented an electrostatic synergistic assembly strategy, to synthesize Cobalt Nickel and Manganese on V_2CT_x MXene denoted as CNMV and explore its application as supercapacitors electrodes. The CNMV electrode yield $1005 Fg^{-1}$ at $1 Ag^{-1}$, thus benefiting from the hetero ion doping effect [31].

Ashish Y et al. in 2022 report a highly electroactive vanadium carbide MXene in a carbon matrix ($V_2CT_x@C$), which was synthesized with the assistance of metal organic frameworks (MOFs). The morphological changes in the stacked nanosheets of V_2CT_x MXene resulted in the formation of exfoliated carbon enriched V_2CT_x nano discs which exhibited improved surface area, conductivity augmented, and enhanced electrode-electrolyte interfacial contact area. This altogether produced a capacitance of $551.43 F g^{-1}$ at $2 Ag^{-1}$ and retained 96.7% of its capacity after 5000 CV cycles demonstrating outstanding cycling stability [32].

2.3. Vanadium Carbides and its composites for electrochemical water splitting

Seung young Park et al. in 2022, modulate electronic structure of V_2CT_x through atomic substitution of Pt in V_2CT_x MXene to promote Pt- V_2CT_x catalytic activity toward HER by lowering the binding force of hydrogen of V_2CT_x through the confinement of Pt atom. In acidic media, the Pt- V_2CT_x has an overpotential of 27 mV at 10mAcm^{-2} demonstrating good catalytic activity [33].

In **2022, Syedah Afsheen et al.** presented material design via introducing multi wall carbon nanotubes (MWCNTs) on V_2CT_x MXene sheets (MWCNT@ V_2CT_x). The MWCNTs catalyst show durability after 16 hours via chronoamperometry test. At 10mAcm^{-2} , the hybrid catalyst yield a minimal over potential of 27mV (HER) and 469 mV (OER) [34].

Jiapei W et al. used a simplistic method to deposit and uniformly anchored nanoparticles of Platinum on the surfaces 2D V_2CT_x MXene to achieve a Pt/ V_2CT_x nanocomposite. In 0.5M H_2SO_4 obtained catalysts-Pt/ V_2CT_x possess a lower Tafel slope is and overpotential of 20.6 mVdec^{-1} and 67 mV respectively [35].

In **2022, Liming Y et al.** through hydrothermal method, constructed Iron Nickel LDH/ V_2CT_x /NF as a self-maintained OER and HER electrode. Strong interaction between the surfaces provided by the constructed nanocomposite provides more active sites, thus improving its electrical conductivity and enhanced mechanical stability. When tested in 1M KOH, the electrocatalyst (FeNi LDH/ V_2CT_x /NF) at 10mAcm^{-2} required just 222 mV for OER) and 151 mV for HER overpotentials [36].

Sin-Yi Pang et al. propose to synthesis V_2CT_x , Cr_2CT_x and Ti_2CT_x via thermal-assisted E-etching method with using HF. The synthesized MXenes were each further decorated with cobalt ions to achieved transitional metal (TM) promoted water splitting catalysts. In 1M KOH their performance in OER remains unchanged for the three catalysts all with overpotential of 420mV at current density of 10mAcm^{-2} . However, for HER, Co^{3+} - Cr_2CT_x (404mV), Co^{3+} - V_2CT_x (460mV) and Co^{3+} - Ti_2CT_x (458mV) at current density of 10mAcm^{-2} [37].

2.4. Cobalt based composites for Electrochemical water splitting

Some recently reported literature on cobalt-based electrocatalyst for water splitting includes Cobalt phosphides (CoP-HS) [38], $CoSe_2/MoSe_2$ nanosheets [39], Ru-CoOx/NF [40], $CuNCo_3$ nanosheets and $CoN_{0.73}Co_3$ nanowires [41], Co-Pi/NiFeOOH/ $BiVO_4$ cobalt oxide (CoOx) [42], heterojunction $Co_3O_4/MXene$ [43], Co^{3+} -decorated MXenes (Co^{3+} - Cr_2CT_x , Co^{3+} - V_2CT_x and Co^{3+} - Ti_2CT_x) [37], CoO/ $CoSe_2$ [44], and hierarchical CoP nanosheet [45].

CHAPTER 3 | EXPERIMENTATION

3.1. Synthesis of MXene

From MAX phase, MXene can be synthesis predominantly via top-down approach and in some cases, bottom-up approaches can be used, and these so far are the two main techniques of fabricating nanomaterials. Similarly, MXene composites can also be synthesized using both bottom-up and top-down approaches [46]. With a suitable liquid solution, mainly HF containing solutions, the A layer in 3D MAX structure can be etch resulting to 2D MXene via top-down approach [14]. Nevertheless, from MAX phase precursors, wet-chemical etching using aqueous HF is commonly used to synthesize MXene.

3.2. Common methods through which MXene composites are synthesized

3.2.1. Solvothermal and Hydrothermal synthesis

Using liquid solvent, mineralizer and precursor at high pressure and temperature, solvothermal and hydrothermal method exploit the interrelationship that exists between them and form a new and desirable nanomaterial [46]. It provides the simplest and most affordable techniques for creating different derivative materials with various structures. The sole difference between hydrothermal and solvothermal method and the is the type of solvent utilized. While hydrothermal methods use water as the solvent, solvothermal methods use organic solvents like ethanol [47]. One-step synthesis, gentle operating conditions, and environmentally friendly and effective solution diffusion are some of its advantages. Additionally, the hydrothermal/solvothermal approach frequently requires less equipment/tools, minute use of energy, and fewer raw materials than other solution preparation. Hydrothermal and solvothermal methods has used to prepare nanocomposites of MXene that includes, CdLa₂S₄/Ti₃C₂ photocatalyst [48], MXene/Ni₃S₂ [49], ZnS/Ti₃C₂ hybrid [50] a layered double hydroxide Ti₃C₂T_x/TiO₂/NiFeCo (TTL)- hybrid [51] and MoS₂ QDs/Ti₃C₂T_x [52].

3.2.2. Co-precipitation method

With the aid of a precipitating agent, often a base in a solvent, metal is precipitated from a salt precursor in the form of hydroxide using the co-precipitation process. To make monodispersed nanomaterial, the controlled release of ions helps to monitor the nucleation and particle growth kinetics. One of the ways that is frequently refer to in the literature for

creating nanoparticles and other composites is co-precipitation. It is highlighted as a straightforward, inexpensive, and quick procedure that is simple to scale up for use in manufacturing applications. It allow the formation of superior (high purity) nanomaterial via hazard-free route [53]. The concentration of the reactants, reaction time, and temperature are crucial for controlling experimental parameters since these affect the precipitation process. Some MXene-based composites prepared through co-precipitation includes synthesis of $\text{MnO}_2/\text{V}_2\text{CT}_x$ [30].

3.2.3. Deposition methods

Deposition processes, including Atomic Layer Deposition-ALD, electrodeposition, photo-deposition, and Chemical Vapour Deposition-CVD and are used to synthesis diverse composites of MXene. The substrate is subjected to many unstable precursors during the chemical vapour deposition (CVD) process, which causes the required material to be deposited on the surface of the substrate, resulting in formation of a thin film. A metal, alloy, semiconductor, or nanocomposite could all be the material that is deposited. MXene hybrids containing metal(transition) phosphides, carbon containing materials and oxides, could be made using electrodeposition techniques. In addition, metallic nano particles such as Cu and Pt, can be deposited by light deposition on the surfaces of MXene. Some deposition techniques used to synthesize MXene-based composites include Pt-TBA- $\text{Ti}_3\text{C}_2\text{T}_x$ [54] and MXene/polypyrrole [55].

3.2.4. Solution processing

For MXene-strengthened polymers, Solution processing is among the commonly used processing methods as a result the hydrophilicity of layered MXene sheets owing to the presence of various functional groups [46]. Here, MXene pre-modified nanomaterials and polymeric materials are normally dispersed in a polar medium consisting N, N-dimethylformamide (DMF), dimethyl sulfoxide-DMSO, and water to enhance the performance [56]. A uniform slurry is created on the mixing of main materials. Through solution processing, MXene with polymers like, polyvinyl alcohol, polyethylene oxide, and polyvinylidene fluoride [35], polyurethane, cellulose [57], and numerous inorganic materials, for example, MOFs, phosphides, TM oxides, chalcogenides been effectively fused with MXenes using this method [58, 59].

Many methods, in addition to the above, that were used in synthesizing composites of MXenes includes, Drop-casting and adsorption [60, 61], Hot pressing techniques [60, 62], In

situ-polymerization blending [60, 63, 64], Mechanical mixing and self-assembly [65-67], solution plasma (SP) method [68], chemical reduction method [43].

3.3. Synthesis and Characterization

Chemicals: Analytical grade chemicals were used and are purchased from Sigma Aldrich. They include Vanadium Aluminum carbide MAX powder (V_2AlC), Potassium Hydroxide (KOH), Deionized water (DI water), Absolute ethanol (35 wt%), Hydrofluoric Acid-HF (50 wt%), Nafion (binder), Carbon Black (CB), Cobalt Nitrate Hexahydrate and Ammonium Hydroxide (NH_4OH).

Equipment and apparatus Required: Apparatus used during chemical etching of MAX powder and as well as the synthesis of doped $Co[NO_3]_2@V_2CT_x$ are as follow:

Teflon beaker, magnetic stirrer, glass beakers, Hotplate, Petri dish, vacuum filtration assembly, pH papers, Sonicator, Centrifuge tubes, centrifuge machine, Digital balance, vacuum drying oven, Filter paper, gas mask, safety gloves, goggle, parafilm, butter paper, micropipette, dropper, and Eppendorf tubes.

3.3.1. Synthesis of multilayer V_2CT_x MXene

Briefly, 1g V_2AlC powder was added gradually (0.2mg/min) into 50 wt% HF solution (20mL) in a Teflon vessel under magnetic stirring (275rpm) at room temperature. After 96h of reaction time, the HF containing dissolve Al solution is transferred in centrifuge tubes(50ml), dispersed in deionized (DI) water and centrifuge for 6 min at 5000 rpm. A dark green supernatant containing HF and dissolve Al is decant and discarded carefully and appropriately. This precipitate is redispersed in DI water and centrifuge (4500rpm for 6min) again for another three cycles to attain a neutral pH. This precipitate is collect using Vacuum-assisted filtration. The wet powder is dried in Vacuum oven at $40^\circ C$ for 12 h to obtain a multilayer V_2CT_x MXene. There was a yield of about 80%.

3.3.2. Synthesis of Cobalt nitrate/Vanadium carbide nanocomposites

Typically, 50 mg V_2CT_x MXene powder dispersed in 25mL DI water and 25mg of $Co[NO_3]_2 \cdot 6H_2O$ in 15ml of DI water where stir separately for 5 minutes. The solutions were joined together and ultra-sonicate for 5 minutes to obtain a uniform solution. Afterwards, the solution is allowed to stir while NH_4OH solution is added gradually using a dropper, to the solution to attain a pH of about 9. This is followed by 3h stirring of the solution at RT. After washing several times with DI water through centrifugation (4500rpm for 5 minutes) and the precipitate collected through vacuum assisted filtration, and dried at $50^\circ C$ for 24h in a vacuum oven. This is labelled as **CoV1**. For comparison, other $Co@V_2CT_x$ nanocomposites

with different cobalt nitrate hexahydrate contents; 7.5mg (CoV2), and 50mg (CoV3) were prepared in the same procedure as CoV1.

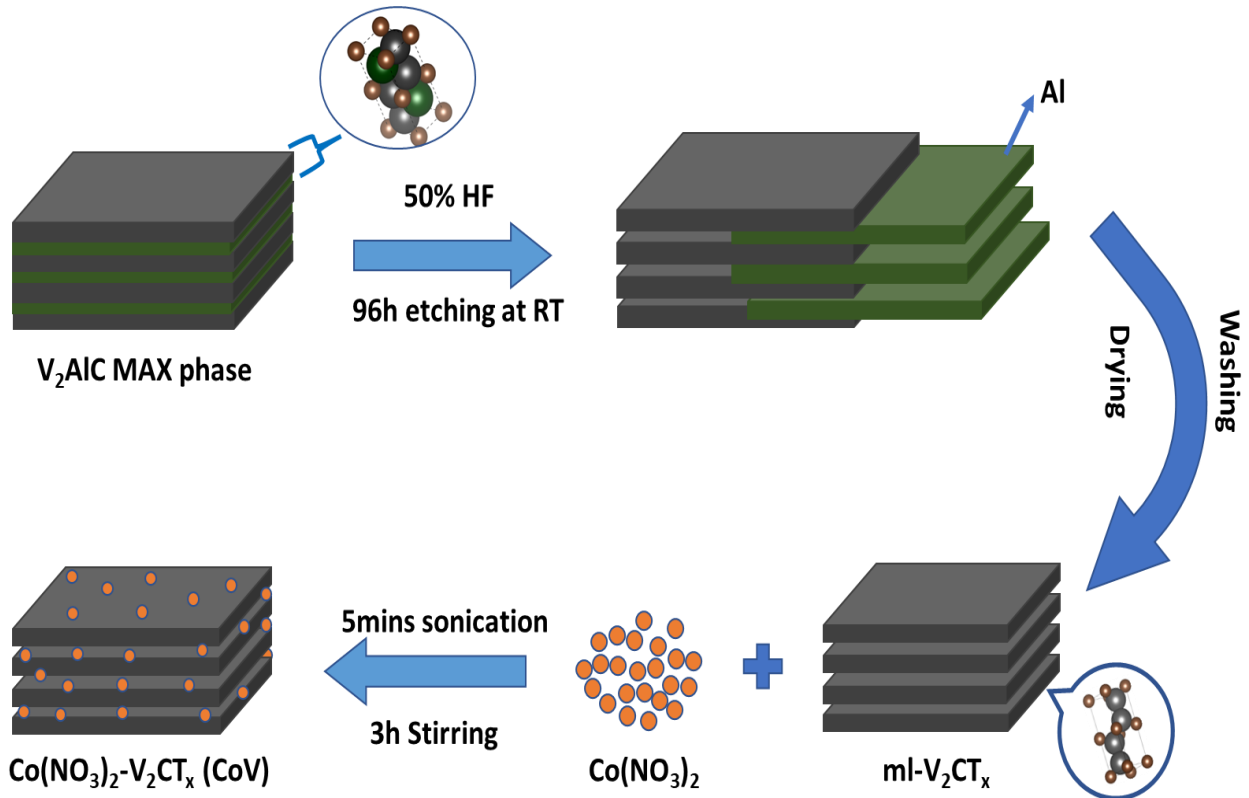


Figure 5: Schematic illustration of V₂CT_x synthesis and anchoring of Co on V₂CT_x sheets

3.3.3. Electrode fabrication

Briefly, 1mg of active mass (Co@V₂CT_x, V₂CT_x or Co), 35ml of nafion (binder) and 100ml ethanol (solvent) in an Eppendorf is sonicated for 10mins to form a uniform slurry. The Nickel form is clean via sonicating in DI water and ethanol for about 10mins each and dried. The slurry is then drop-cast on Nickel form (1cm²) and dried in an oven overnight. The electrode is pressed at 500 psi for about 10 seconds.

3.4. Characterizations tools

To determine/identify the particle size, phase, structure, the functional groups, specific area of the surface, morphology, composition, and thermal stability of the Co, V₂CT_x, and Co@V₂CT_x are characterized through techniques such as

- ❖ Thermogravimetric Analysis/ Differential Scanning Calorimetry (TGA/DSC)
- ❖ Raman Spectroscopy (Raman)

- ❖ X-Ray Diffraction (XRD)
- ❖ Fourier Transform Infrared Spectroscopy (FTIR) and
- ❖ Scanning Electron Microscopy (SEM)/ Energy Dispersive X-ray (EDX)
- ❖ Cyclic Voltammetry

3.4.1. X-ray Diffraction (XRD)

The main use of XRD analysis is to recognize materials established by their diffraction pattern. Moreover, apart from phase identification, XRD also gives data on how the real structure varies from the perfect structure, due to internal stresses and defects.

Working Principle: When light waves of sufficiently small wavelength reach the lattice, they are diffracted from the points of the lattice. At specific incident angles, the bent parallel waves interfere with each other and generate peaks with intensity. Arrays of regular pattern refers to Crystals while electromagnetic radiation in the form of waves is referred to as X-rays. Through the interaction with atom's electron, incident x-rays are scattered by crystal atoms, resulting to a phenomenon called elastic diffusion. A evenly diffused array creates a normal spherical wave array. Through destructive interference, the waves in some direction cancel each other, and in some cases, they complement each other constructively in specific paths as defined by Bragg's Law:

$$2 d \sin \theta = n \lambda$$

Where,

d denotes the distance between the diffraction planes

θ represents the incidence angle

n is representing an integer

λ denotes wavelength of the beam.

The exact directions that seem like points on the spreading pattern are termed reflections. Thus, XRD patterns are the consequence of electromagnetic rays hitting a well scattered array. Electromagnetic rays are utilized to generate diffraction images since they possess a wavelength (**λ**) that is approximately equal to the distance(**d**) between the crystal. Diffraction arises only when Bragg's law fulfills the requirement for generating interference of planes with distance d.

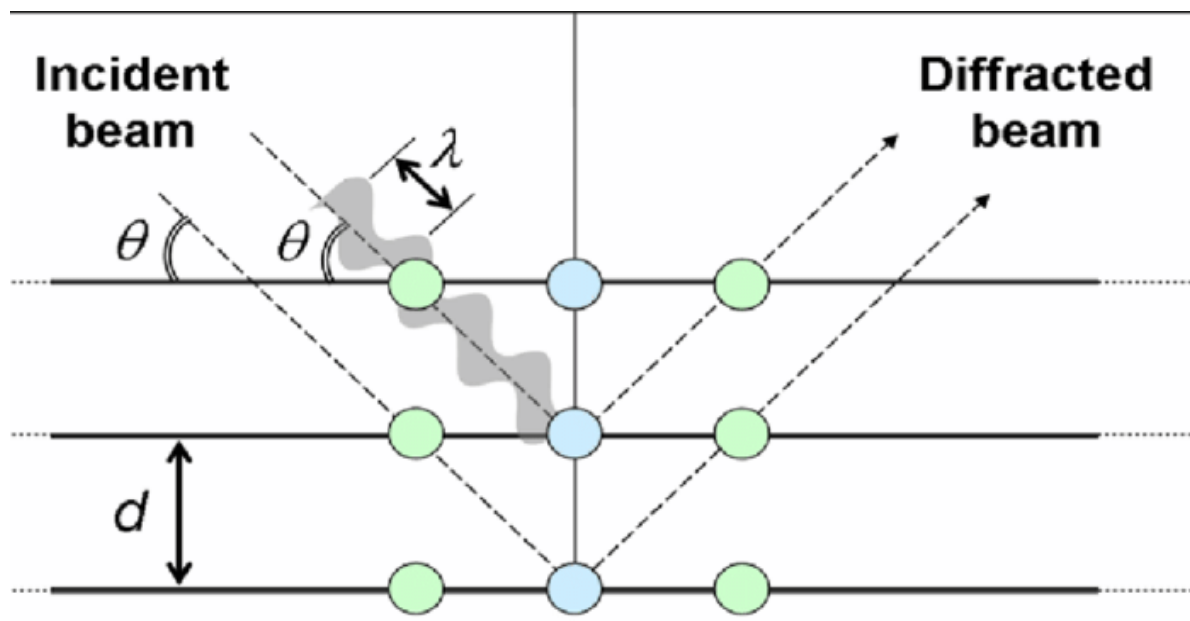


Figure 6: Illustration of diffraction rays and Bragg's law [69].

Application: XRD is a technique that does not destroy the sample and is primarily used to

1. Determine crystal orientation and phases of crystal or grain.
2. Define structural properties such as size of grain , parameters of the lattice, tension, and composition of phase.
3. Measure multi-layer and film thickness as well as the average distance between layers or rows of atoms.
4. Determine the atomic arrangement.

3.4.2. Scanning Electron Microscopy (SEM) and Energy Dispersive X-ray (EDX)

Through SEM, 2D image are produces by examining the surface of sample with a concentrated electron beam . Through the interaction of electrons and atoms in the sample, signals are produced that comprise information regarding the surface composition and topography of the sample.

Working principle

Works on the principle of electron scattering at the sample surface. Electrons from the source/electron beam (primary electrons) are directed towards the sample surface in a raster sweep pattern. The electron transfers part of its energy to the sample, which is then emitted to the sample surface.

The excited electrons from the sample then produce signals in the form of backscattered electrons, secondary electrons (SE) and characteristic X-rays containing information about the sample. Multiple recorded SEs resulted in brighter points of the image being formed,

some recorded SEs resulted in blurry or gray spots, and none resulted in dark spots. This is done row by row until the entire surface of the scanned sample forms a rectangular image on the screen.

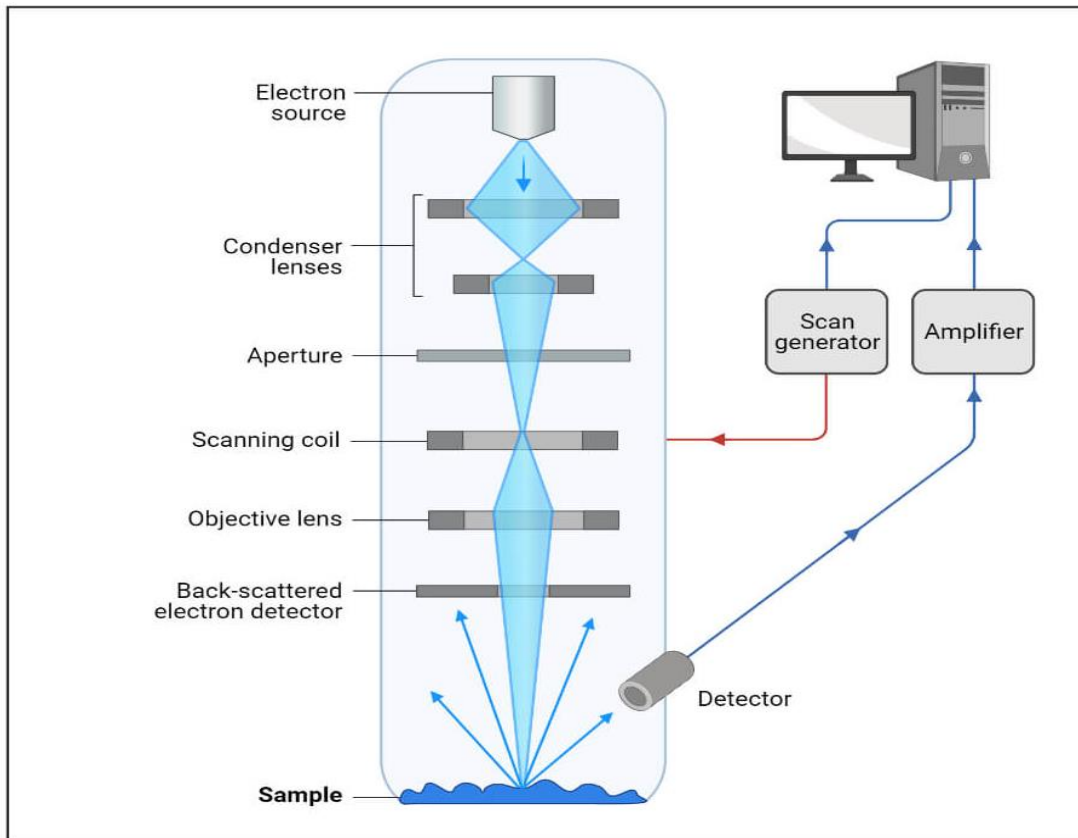


Figure 7: Parts of the SEM showing internal structure [69].

Energy Dispersive X-ray Spectroscopy- EDX

It process of acquiring and characterizing X-rays to determine the chemical composition of a sample. When PE knocks electrons out of the atom's K shell, an empty spot remains, creating an unstable state. Outer shell electron falls to fill up the empty space, releasing a characteristic X-ray photon. X-ray energy is produced due to the difference in ionization energies of electrons during a transition and is specific to a particular element.

3.4.3. Raman Spectroscopy (Raman)

A non-destructive chemical analysis technique, Raman spectroscopy gives detail knowledge about crystallinity, chemical structure, molecular interactions and phase . Raman is employed to analyze a wide range of samples that includes, solids, slurries, powders, liquids, gels, inorganic, metal oxides amongst others.

Working principle

It is centered on the interaction of chemical bonds with light in the material. When

monochromatic radiation reaches the sample surface, it can be scattered, absorbed, or reflected in one way or another. **Rayleigh scattering**, which comprises of about 90% of the scattering, has the same wavelength as the laser source, and gives no beneficial information. The remaining scattering constitutes **Raman scattering** and they have different wavelength to that of the laser source. Raman scattering is divided into **Stokes scattering** (energy of incident photon greater than that of the scattered photon) and **Anti-Stokes Raman scattering** (energy of incident photon less than that of the scattered photon). Raman spectrum (determined by plotting the intensity of this "shifted" light against the frequency that gives the sample's Raman spectrum).

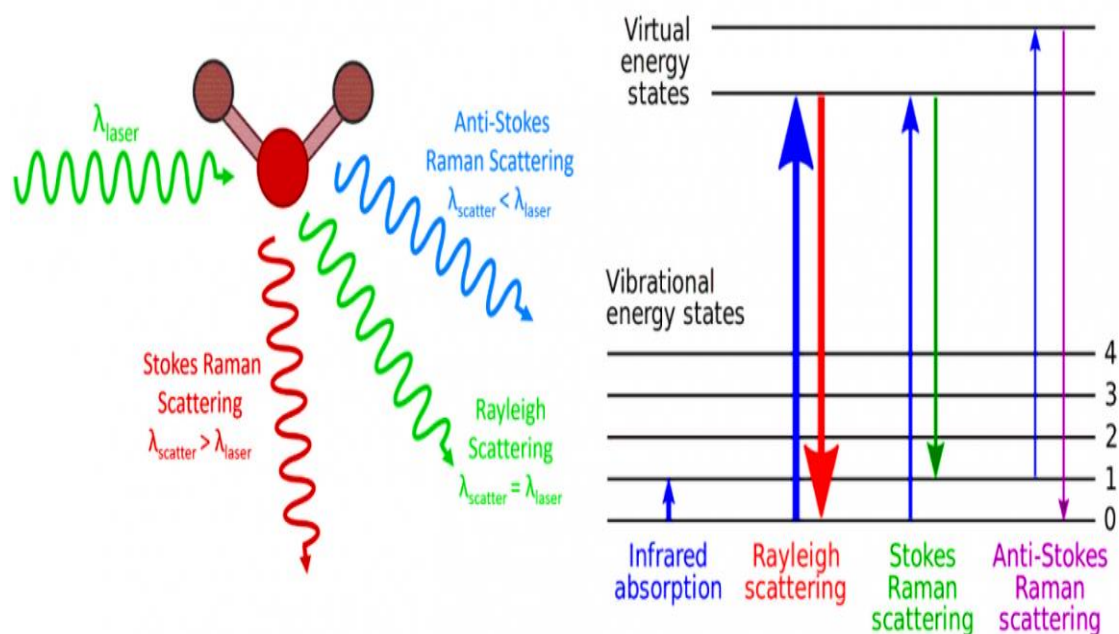


Figure 8: Schematics Illustration of the working principle of Raman [70]

3.4.4. Fourier Transform Infrared Spectroscopy-FTIR

FTIR operates using infrared spectroscopy and due to its high speed, precision, improved sensitivity, does not destroy samples and is easy to operate, it is preferred over other dispersive spectrometers.

Working principle

Infrared spectroscopy technology is centered on the atomic vibrations of a molecule that absorb only certain energies and frequencies of radiated infrared. Molecules can be identified and categorized by FTIR because various molecules will have distinct infrared spectra. The radiations are then passed by the interferometer. The different wavelengths of

Infrared beam are then absorbed by the sample according to its chemical properties. The energy difference in the absorbed beam is then detected by the detector. The signal from the detector is amplified by the amplifier and converted to digital signal by analog-to-digital converter. The signal is then transferred to a computer in which Fourier transform is carried out.

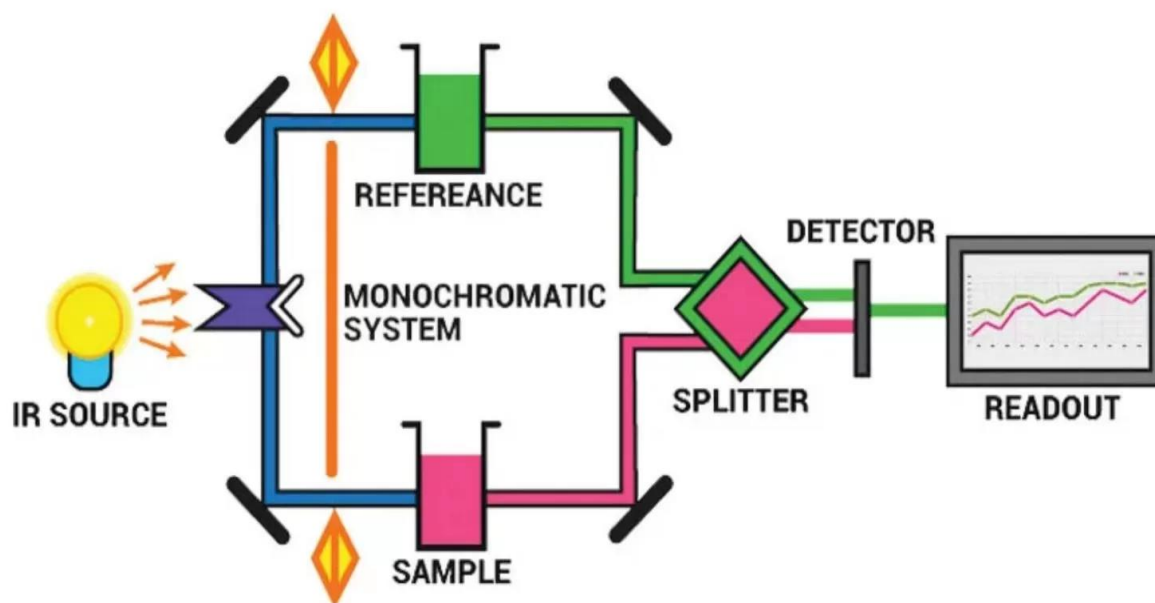


Figure 9: Schematic showing the working principle of FTIR [76]

3.4.5. Thermogravimetric Analysis/Differential Scanning Calorimetry (TGA /DSC)

Using Differential Scanning Calorimetry and Thermogravimetric Analysis, the mass and heat flow rate of a sample is examined as a function of temperature or time when the specimen is exposed to a temperature in a controlled environment resulting to an increase or decrease in weight material is heated.

DSC/TGA consist of a specimen holder backed by a precision balance. This pan sits in the oven and is cooled or heated throughout the experimentation. A sample of bleach gas controls the sample medium. A reactive or/and inert gas flows through the sample and leaves via the exhaust.

DSC/TGA can calculate solvent, plastic, and water loss. Also, oxidation, decomposition, pyrolysis and fractions weight percentage.

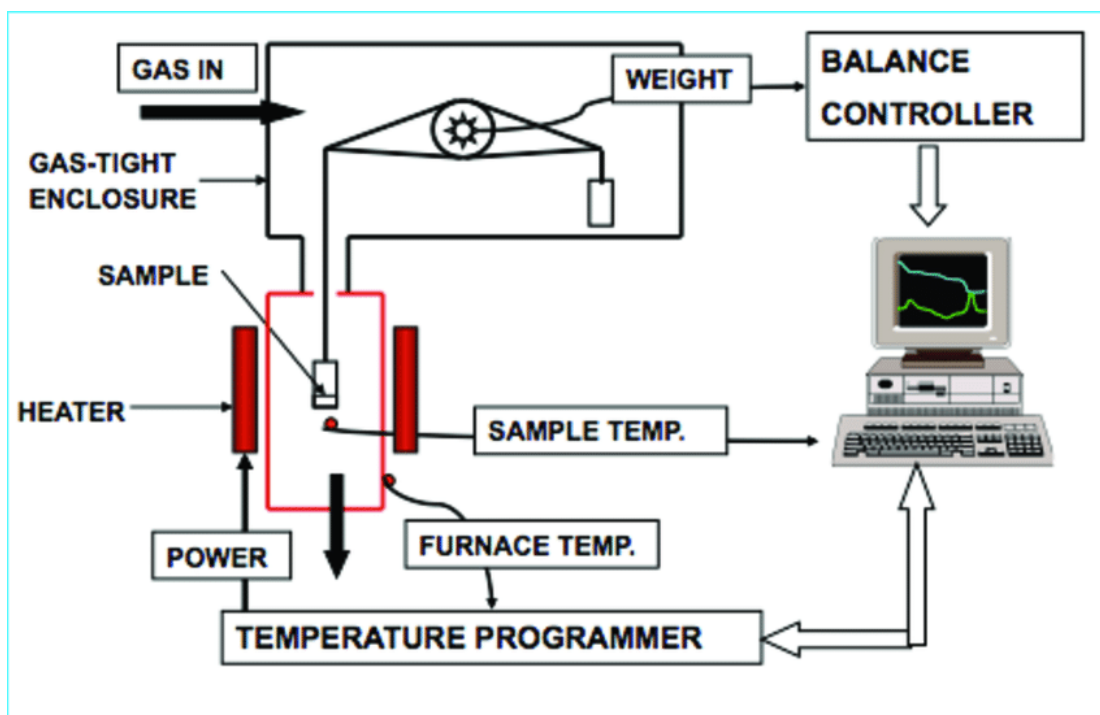


Figure 10: Schematic diagram showing parts of the thermogravimetric analysis instrument [71].

3.5. Electrochemical Measurements

All electrochemical tests have been conducted on 1010B Potentiostat by Gamry electrochemical workstation in 1.0M KOH electrolyte, utilizing a three-electrode system. The working electrode consists of Co, V_2CT_x and $Co@V_2CT_x$ nanocomposites supported on nickel foam as the reference electrode is of Ag/AgCl and platinum wire for the counter electrode. For **Linear Sweep voltammetry**, all potentials standardized against reversible hydrogen electrode (RHE) using Nerst equation as $E_{RHE} = E_{Ag/AgCl} + 0.0591pH + 0.205$ and both OER and HER were tested at a constant 10 mVs^{-1} scan rate.

Electrochemical Impedance Spectroscopy was run at frequency from 20KHz to 0.1 Hz under open circuit potential using a sinusoidal signal of 10mV.

Cyclic voltammetry voltammograms were taken at 100, 50, 20, 10, 5 and 2 mVs^{-1} .

From CV test, the gravimetric capacitance (Fg^{-1}) was calculated by using equation

$$C_s = \int I(V)dV/mV\Delta V \dots\dots\dots(1) [28]$$

Where

I represent current

V stands for scan rate used

m represents the active mass loading of electrode

ΔV denotes voltage window.

Also, using GCD data, the following were calculated :

$$\text{Specific charge capacity (Ahg}^{-1}\text{)} = \frac{\Delta t \times I}{m} \dots\dots\dots(2)$$

$$\text{Gravimetric specific capacitance (F g}^{-1}\text{)} = \frac{I \times \Delta t}{m\Delta V} \dots\dots\dots(3)$$

$$\text{Energy density (Wh kg}^{-1}\text{)} = \frac{C_s \times \Delta V^2}{2 \times 3.6} \dots\dots\dots(4)$$

$$\text{Power density} = \frac{3600 \times E}{\Delta t} \dots\dots\dots(5) [72].$$

where ΔV (V) is the voltage window, and Δt (s) is the discharge time.

CHAPTER 4 | RESULTS AND DISCUSSION

4.1. Results from Characterization tools

4.1.1. X-Ray Diffraction

The XRD patterns for V_2AlC , V_2CT_x and $Co@V_2CT_x$ are shown in figure 11. The crystal planes (002) and (103) of V_2AlC are found at 13.5° and 41.3° respectively (PDF#29-0101). The peaks at 13.5° and 41.3° drastically reduced in intensity, indicating tiny quantity of the MAX phase that are unetched, as suggested in earlier studies [32]. The peak (002) is lowered to 8.9° , implying that Al in V_2AlC is removed, resulting to V_2CT_x , and further the d-spacing increase to 9.8 \AA . The anchoring of Co on V_2CT_x causes a further shift of the (002) peak to a position at about 7.5° with a corresponding d-spacing of 11.7 \AA as indicated in figure 14. The peaks at 35.57° , 42.6° and 61.67° match the planes (111), (200), and (220) respectively of Co (PDF#040-0363). This is in conformity with the EDAX in figure 15e, showing the weight percent of elements present in V_2CT_x the $Co@V_2CT_x$ composites.

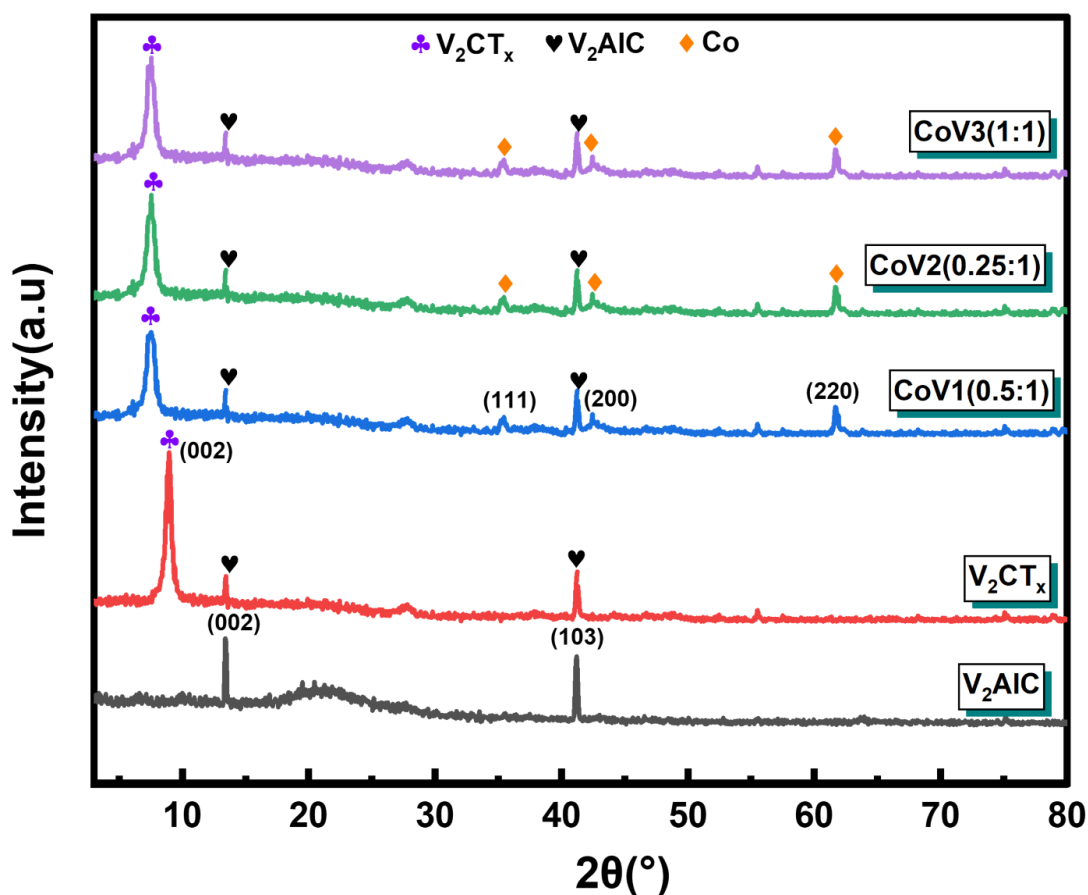


Figure 11: XRD of etched V_2CT_x , and various $Co@V_2CT_x$ composites

4.1.2. Scanning Electron Microscopy (SEM) and Energy Dispersive X-ray (EDX)

The structure and morphology of V_2CT_x , and $Co@ V_2CT_x$ were investigated by SEM. Figure 12a show unetched V_2AlC MAX phase and figure 12b unveils the SEM image of MXene (V_2CT_x), which shows that V_2CT_x sheets opens after etching. Figure 12c present the image of $Co@ V_2CT_x$ composite with Co particles uniformly coated on and in between V_2CT_x sheet. The elemental mapping on selected region of the nanocomposites (in figure 12d) signifies the existence of V, O, C, Al, Co, and F. The weight percent of elements present in etched V_2CT_x and $Co@ V_2CT_x$ is shown in figure 12e. The less weight of Al indicates the successful synthesis of V_2CT_x MXene from Precursor V_2AlC MAX phase.

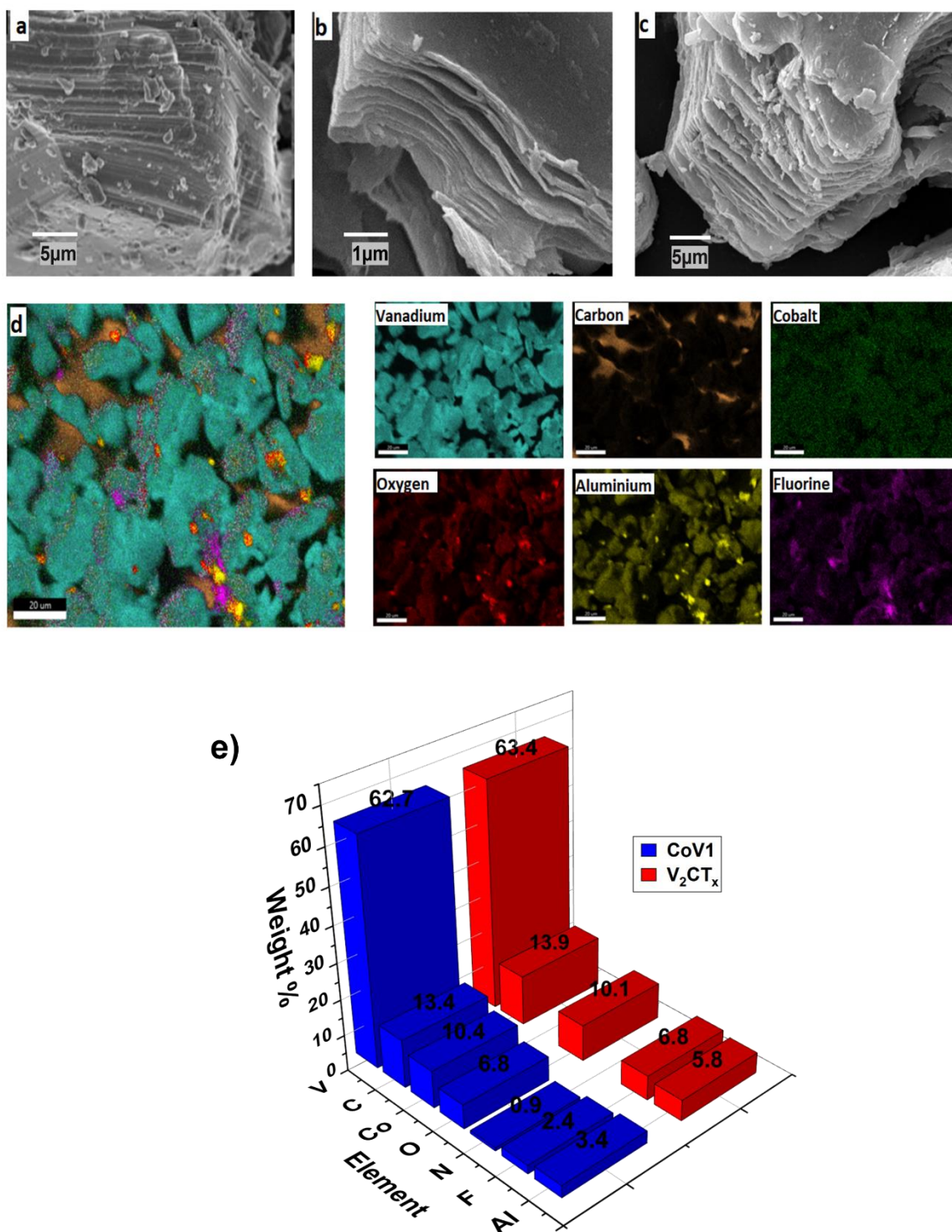


Figure 12: Micrographs from SEM of a) V_2AlC b) V_2CT_x MXene, and c) $Co@V_2CT_x$ d) element mapping of $Co@V_2CT_x$ nanocomposites showing the presence and distribution of V, C, Co, O, Al, and F e) EDX show the percentage weight of elements in V_2CT_x MXene, and $Co@V_2CT_x$

4.1.3. Raman Spectroscopy

Raman spectra in figure 13 was utilized to evaluate the phase transformation and structure of V_2AlC , etched MXene(V_2CT_x), Cobalt and $Co@V_2CT_x$ composite. The vibrations associated within V-Al bond in the MAX phase is located around 350cm^{-1} , disappear in the etched V_2CT_x resulting to new peaks within 264cm^{-1} to 610cm^{-1} hence indicating the successful removal of the Al in V_2AlC to form V_2CT_x . This is supported by the vibrations at 410 cm^{-1} , as a result of $V_2C(OH)_2$ signifying out-of-plane V-atom vibrational modes, while the remaining two peaks are due to the A_{1g} mode of MXene matching to V_2CF_x and $V_2CO(OH)_2$, respectively, corroborating further the etching of MXene with the existence of surface terminations such as O, OH, and F [73]. The increased interlayer spacing in V_2CT_x is shown by vibrational peaks at frequency of 264cm^{-1} . The two prominent peaks of Co appear at 126cm^{-1} and 1046cm^{-1} . In the $Co@V_2CT_x$ nanocomposite, additional movement of peaks is seen along with the widening of peaks at 262 cm^{-1} , 423 cm^{-1} , and 608cm^{-1} , which can be related to the bond of Co over the surface of V_2CT_x MXene[74, 75].

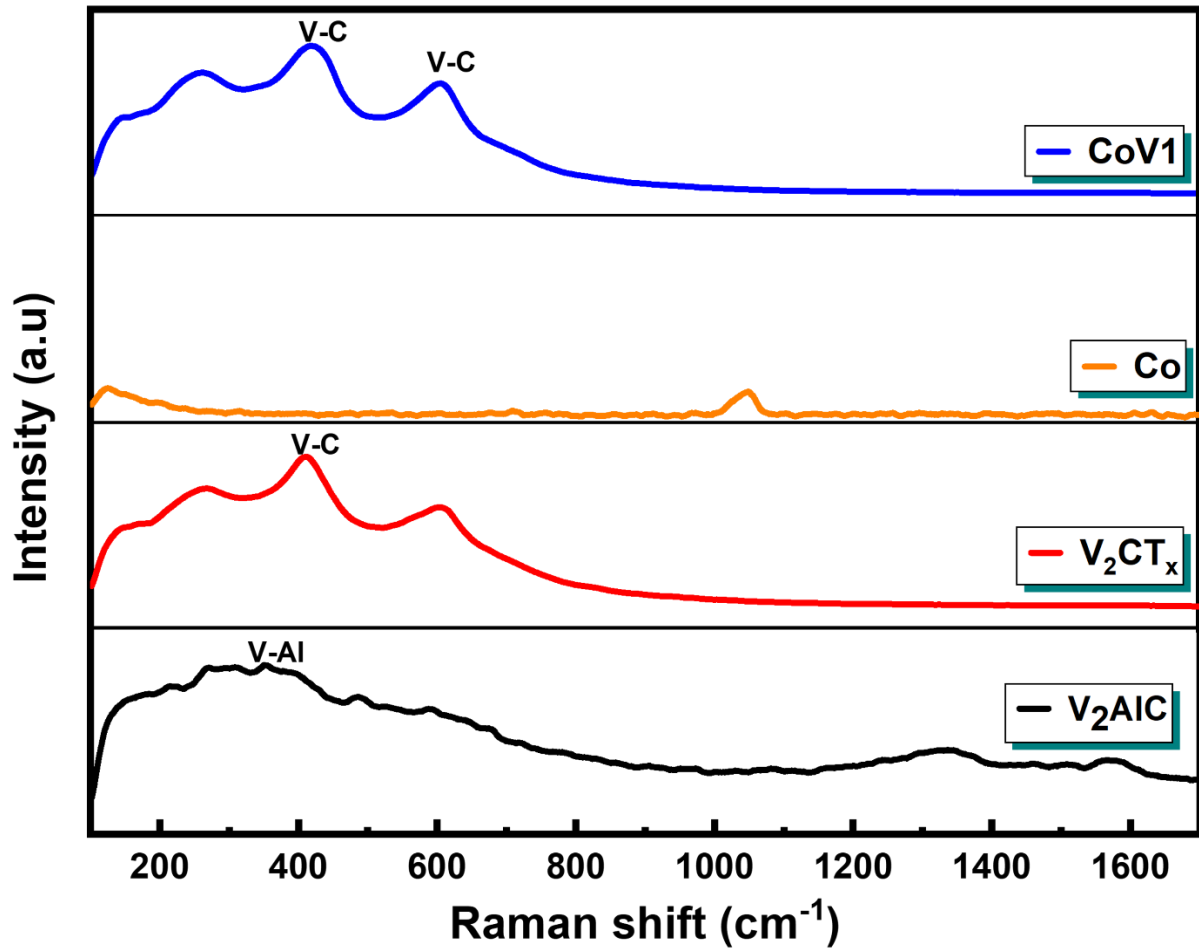


Figure 13: Raman spectra for V_2AlC , V_2CT_x , Co and $Co@ V_2CT_x$

4.1.4. Fourier Transform Infrared Spectroscopy

The Infrared spectra plot for etched V_2CT_x and $Co@ V_2CT_x$ nanocomposites is illustrated in figure 17. The peak located around 3427cm^{-1} represents the C=C bond and the C=O vibration is represented around 1630cm^{-1} . The FTIR spectra of etched V_2CT_x and $Co@ V_2CT_x$ nanocomposites show a broad peak between 3200 and 3600cm^{-1} , possibly as a result of the O–H stretching vibration. Furthermore, the infrared band around 585cm^{-1} is the characteristic V–O broadening vibration. The absorption bands of $Co@ V_2CT_x$ (CoV_1 , CoV_2 and CoV_3) are almost the same as those of V_2CT_x in the IR spectrum, which indicates that the $Co@ V_2CT_x$ nanocomposite material is formed.

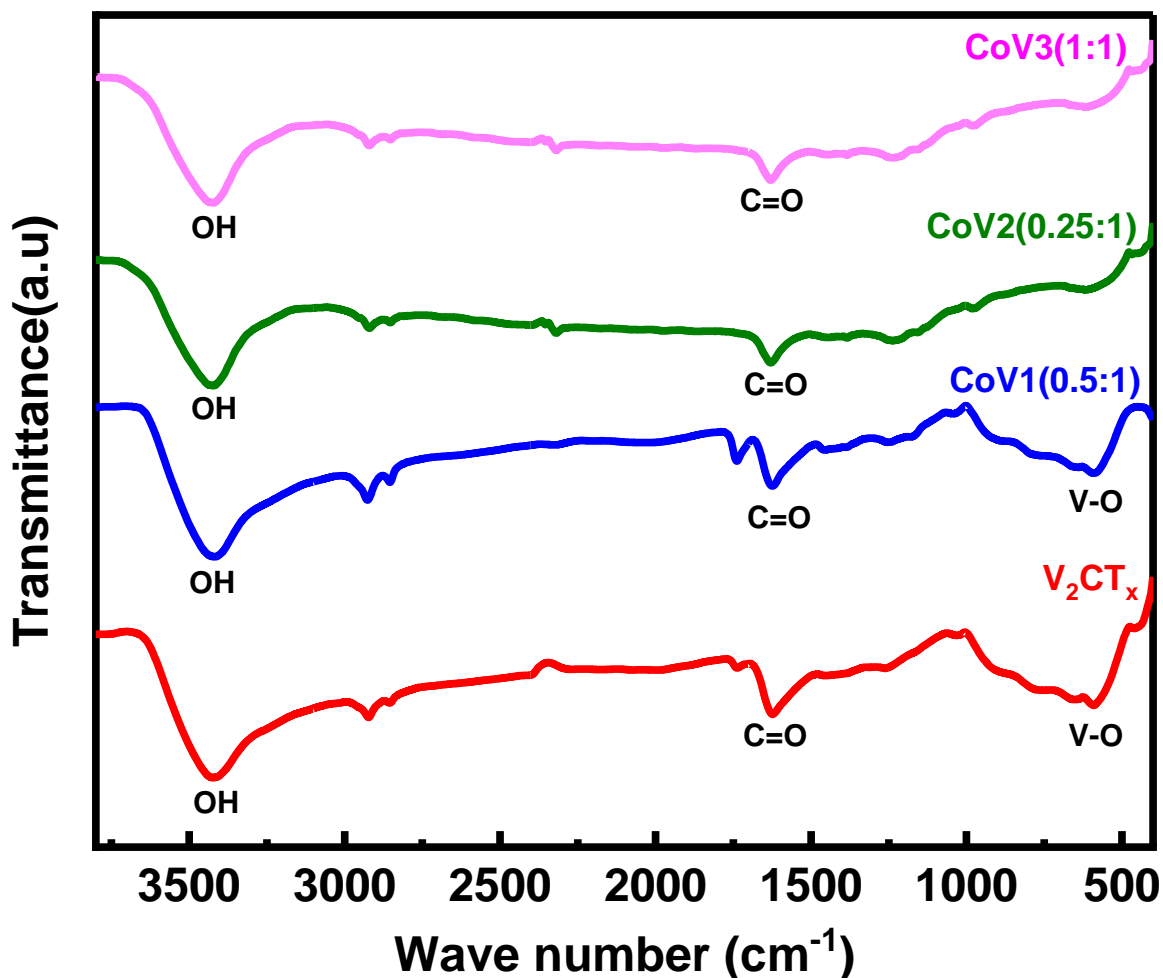


Figure 14: FTIR showing V₂CT_x and various samples of Co@V₂CT_x

4.1.5. Thermogravimetric Analysis/Differential Scanning Calorimetry (TGA/DSC)

Figure 15a and 15b present the TGA curves for etched MXene and Co@V₂CT_x in a Mixture of air and Nitrogen atmosphere.

For the pristine V₂CT_x (figure 18a), there was drastic weight loss of about 73% within a temperature range of 0°C to 241°C. Since the V₂CT_x was synthesized via wet chemical etching using HF, its surface has possibly OH, F and/or O, termination [13]. At high temperature, OH and F terminations are lost or replaced with O. Hence the weight loss could be due to the loss of water adsorbed in the form of moisture and HF on V₂CT_x surface. This leaves the V₂CT_x MXene with o-termination, stable for next 300°C. The DSC curves (red) indicate that the heat flow was mainly endothermic before reaching 300°C. At this stage the sample is absorbing heat to vaporize moisture in the sample which is manifested by a huge weight loss on the TGA curve. After 300°C, the heat flow out of the sample (exothermic) as there is little or reaction going on but a phase change.

The Co@V₂CT_x (figure 15b) is more stable and there was no significant weight loss. There was a total of about only 17% weight loss. This could be due to the evaporation of the moisture from the Co(NO₃)₂·6H₂O before it attains crystal form. The DSC curves (red) shows that the heat flow was entirely endothermic, absorbing heat to vaporize moisture and volatile materials in the sample.

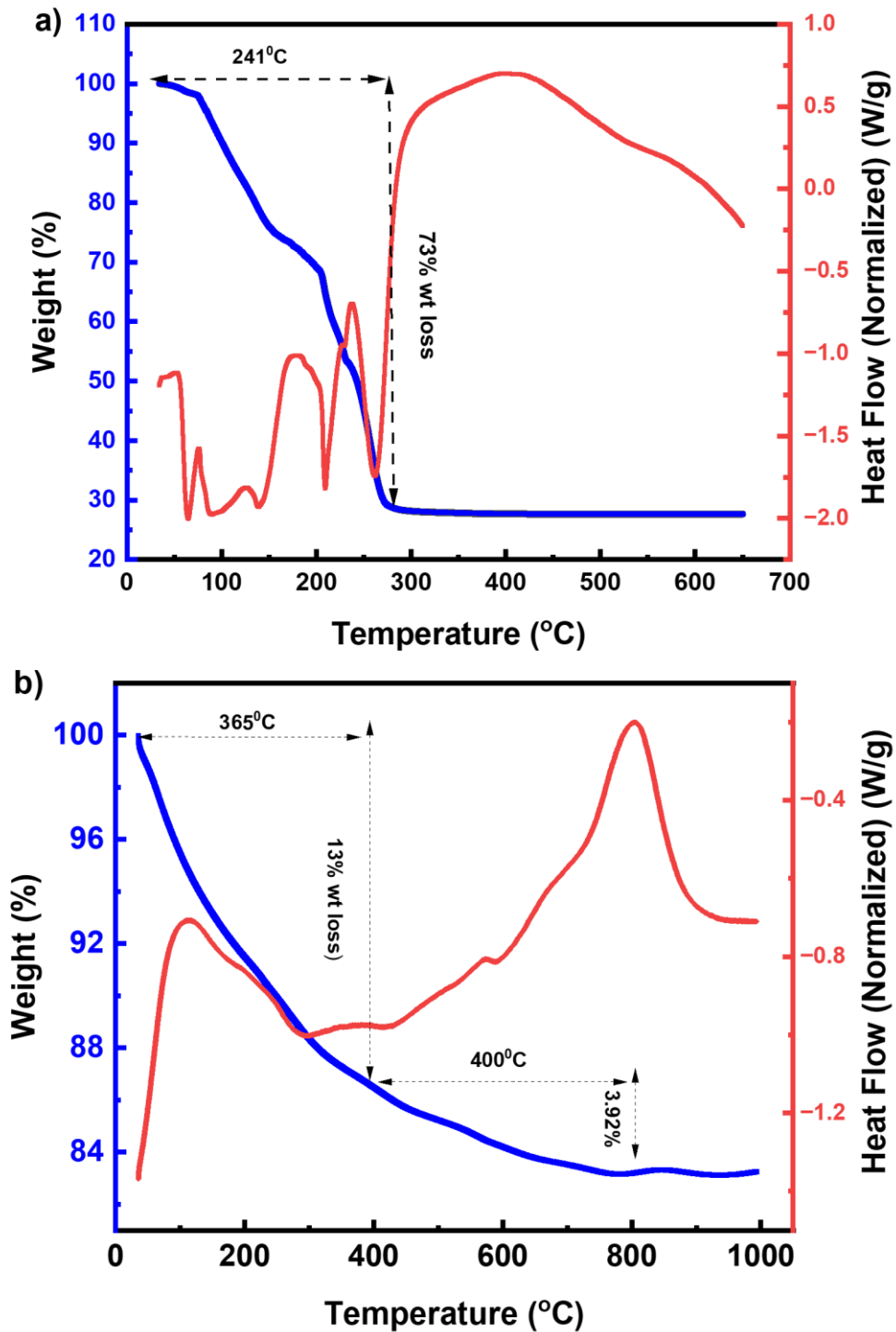


Figure 15: TGA/DSC plot for a) V₂CT_x and b) Co@V₂CT_x nanocomposite

4.2. Electrochemical characterization and measurements

4.2.1. Cyclic voltammetry

Cyclic voltammetry voltammograms were taken at 100, 50, 20, 10, 5 and 2 mVs⁻¹.

From CV test, the gravimetric capacitance (Fg⁻¹) was calculated by using equation

$$C_s = \int I(V)dV/mV\Delta V \dots\dots\dots(1) [28]$$

Where

I represent current

V stands for scan rate used

m represents the active mass loading of electrode

ΔV denotes voltage window.

Figure 19 shows the CV curve of the etched V₂CT_x within a voltage window of 0.4V (0.15V to 0.55V). There are nearly symmetric redox peaks at all scan rate, thus manifesting a good electrode activity. The gravimetric specific capacitance was 318 Fg⁻¹ at 2mVs⁻¹, 274 Fg⁻¹ at 5mVs⁻¹, 241 Fg⁻¹ at 10mVs⁻¹, 204 Fg⁻¹ at 20mVs⁻¹, and 148 Fg⁻¹ at 50mVs⁻¹.

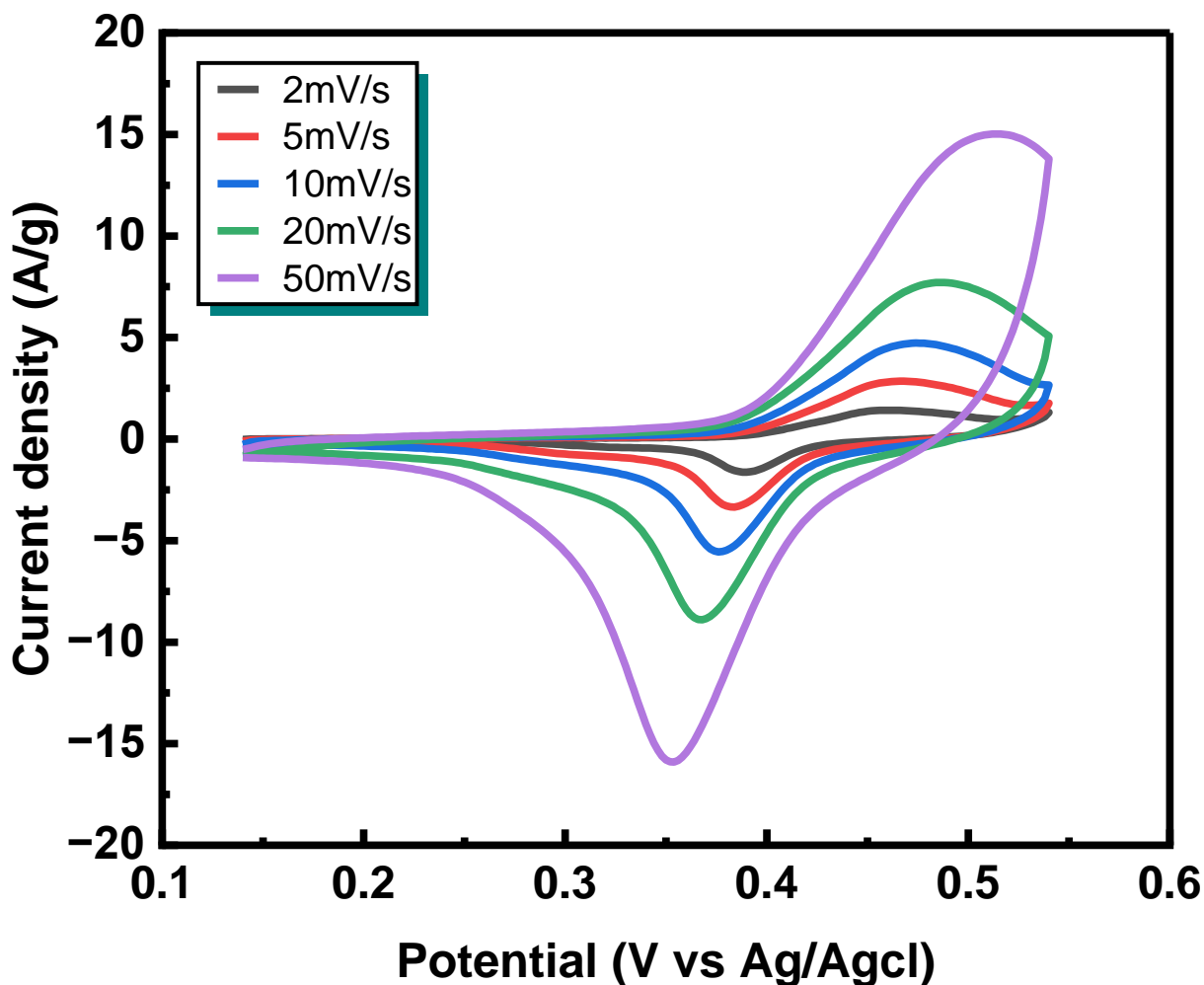


Figure 16: Voltammograms of V₂CT_x for different scan rates

The growth of Cobalt on V₂CT_x was done in three mass ratios of Cobalt to V₂CT_x as CoV1(0.5:1), CoV2(0.25:1) and CoV3(1:1). With a voltage window of 0.75V (-0.15 to 0.6V), CoV1 produced the best results, as a result of synergistic effect of the nanocomposites formed. At scan rates of 2mVs⁻¹, the specific capacitance is 1259Fg⁻¹, hence increased by three folds as compared to the etched V₂CT_x. For various scan rates, the CV curves have pairs of nearly symmetric oxidation (up) and reduction (down) showing existence of Faradaic reaction which a reversible electrochemical process. As shown in figure 16 and 17, a gradually increase of the redox peaks was observed as the scan rates increases (2mVs⁻¹ to 50mVs⁻¹), implying the swift boost of ions and electrons transfer between the interface of electrode and electrolyte.

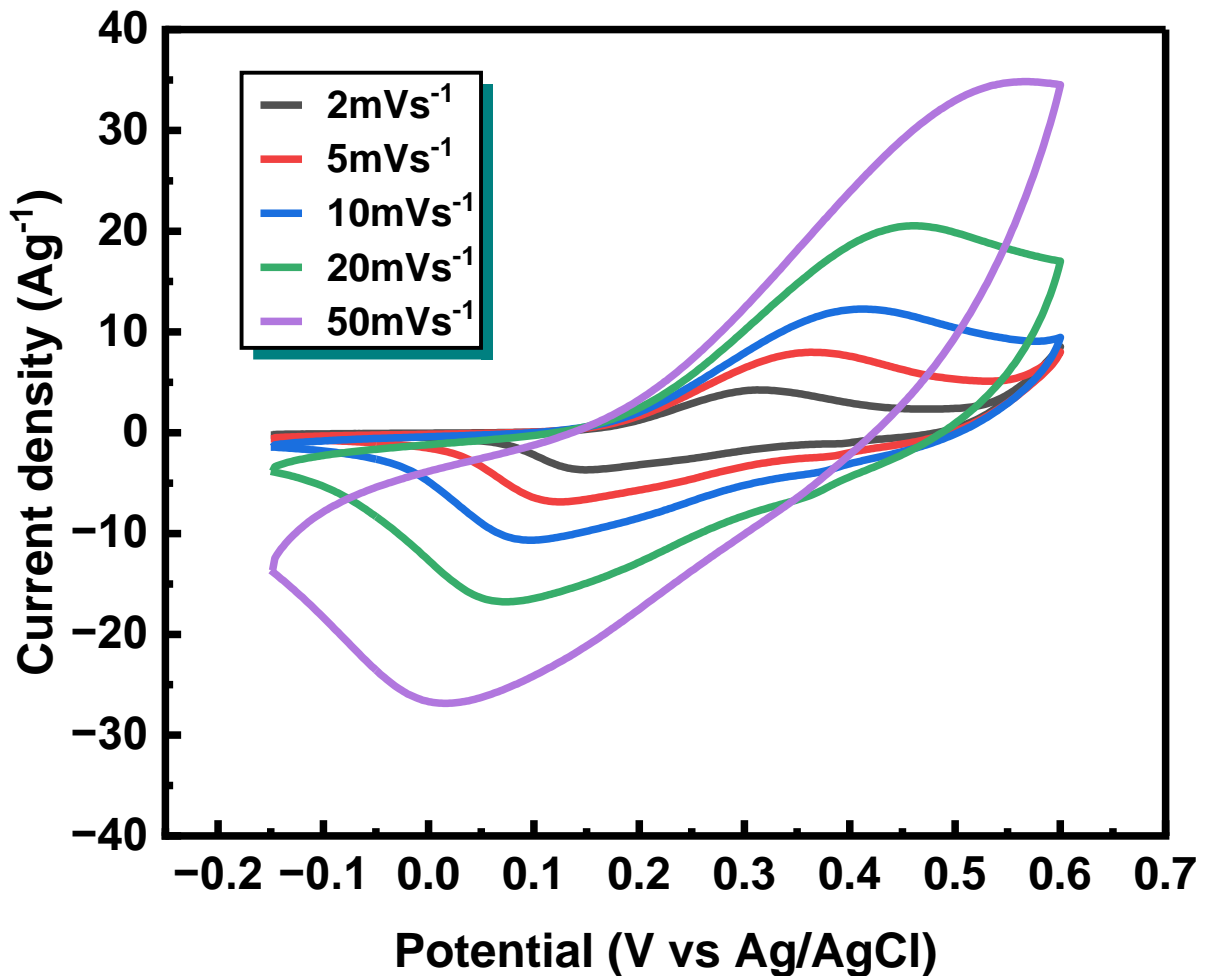


Figure 17: CV curves of Co@ V₂CT_x (CoV1) at different scan rates

Other nanocomposites of Co@V₂CT_x includes CoV2 and CoV3 producing 852Fg⁻¹ and 589Fg⁻¹ at scan rate of 2mV⁻¹ respectively.

Also, when the Co supported on Nickel foam was tested over a voltage window of 0.75V, it yields a capacitance of 612Fg⁻¹ at 2mVs⁻¹.

Figure 18 present a variation of scan rates with specific capacitance of V₂CT_x, Co and various samples nanocomposites of Co@V₂CT_x (CoV1, CoV2 and CoV3). The capacitance declines as the scan rates increases from 2mVs⁻¹ to 50mVs⁻¹.

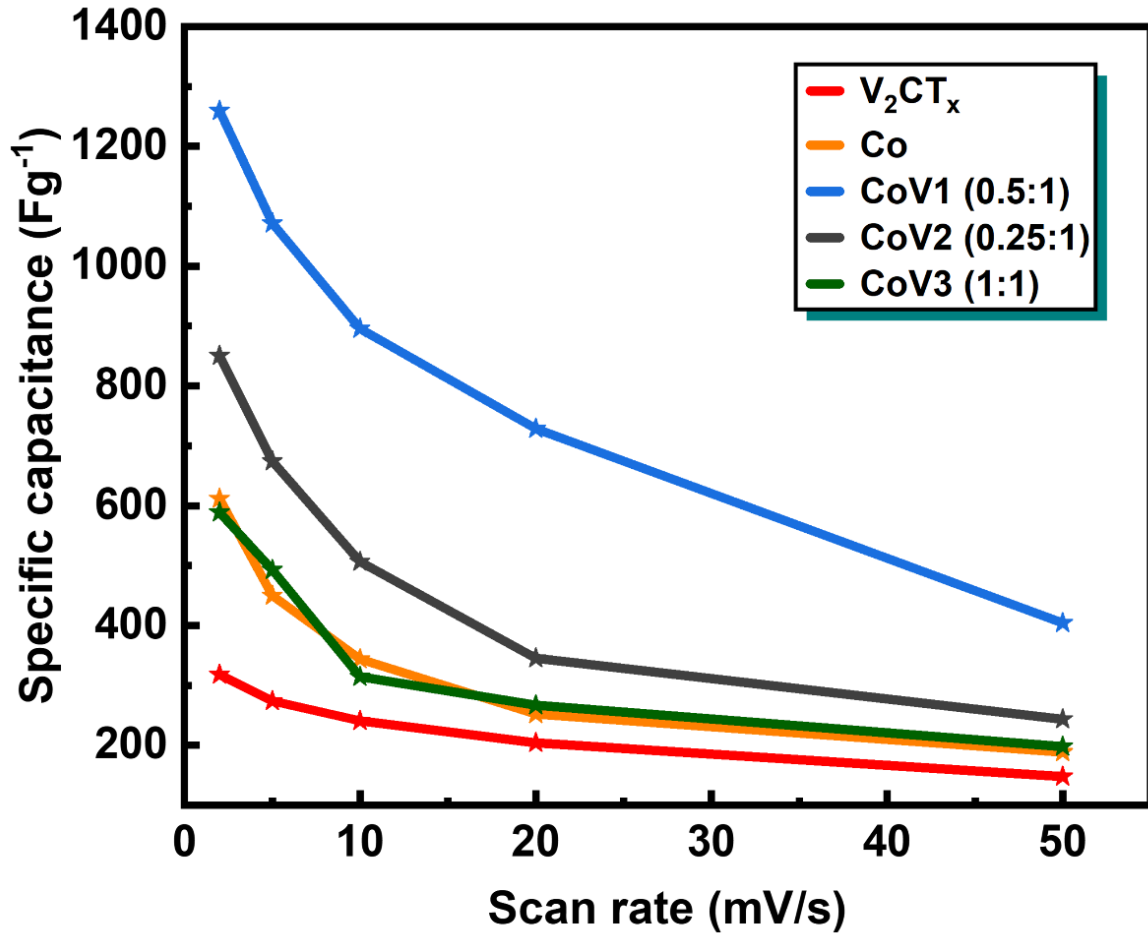


Figure 18: Scan rate vs Specific capacitance of various samples.

4.2.2. Galvanostatic Charge Discharge (GCD)

The GCD curves were taken at 10, 5, 2, and 1Ag⁻¹ within a potential window of 0.65V (figure 22). The Specific charge capacity , gravimetric specific capacitance , Power, and Energy density were determined employing equation 2- 5:

$$\text{Specific charge capacity (Ahg}^{-1}\text{)} = \frac{\Delta t \times I}{m} \dots\dots\dots(2)$$

$$\text{Gravimetric specific capacitance (F g}^{-1}\text{)} = \frac{I \times \Delta t}{m \Delta V} \dots\dots\dots(3)$$

$$\text{Energy density (Wh kg}^{-1}\text{)} = \frac{C_S \times \Delta V^2}{2 \times 3.6} \dots\dots\dots(4)$$

$$\text{Power density} = \frac{3600 \times E}{\Delta t} \dots\dots\dots(5) \text{ [72].}$$

where ΔV (V) denotes the voltage window, and Δt (s) represent the discharge time.

At 1Ag^{-1} , 2Ag^{-1} , 5Ag^{-1} and 10Ag^{-1} current densities, the specific capacitance was 493F g^{-1} , 372F g^{-1} , 317F g^{-1} and 268F g^{-1} respectively. Has a specific charge capacity of 82.2 Ahg^{-1} , energy, and power density of 26.7Whkg^{-1} and 325Wkg^{-1} at 1Ag^{-1} respectively.

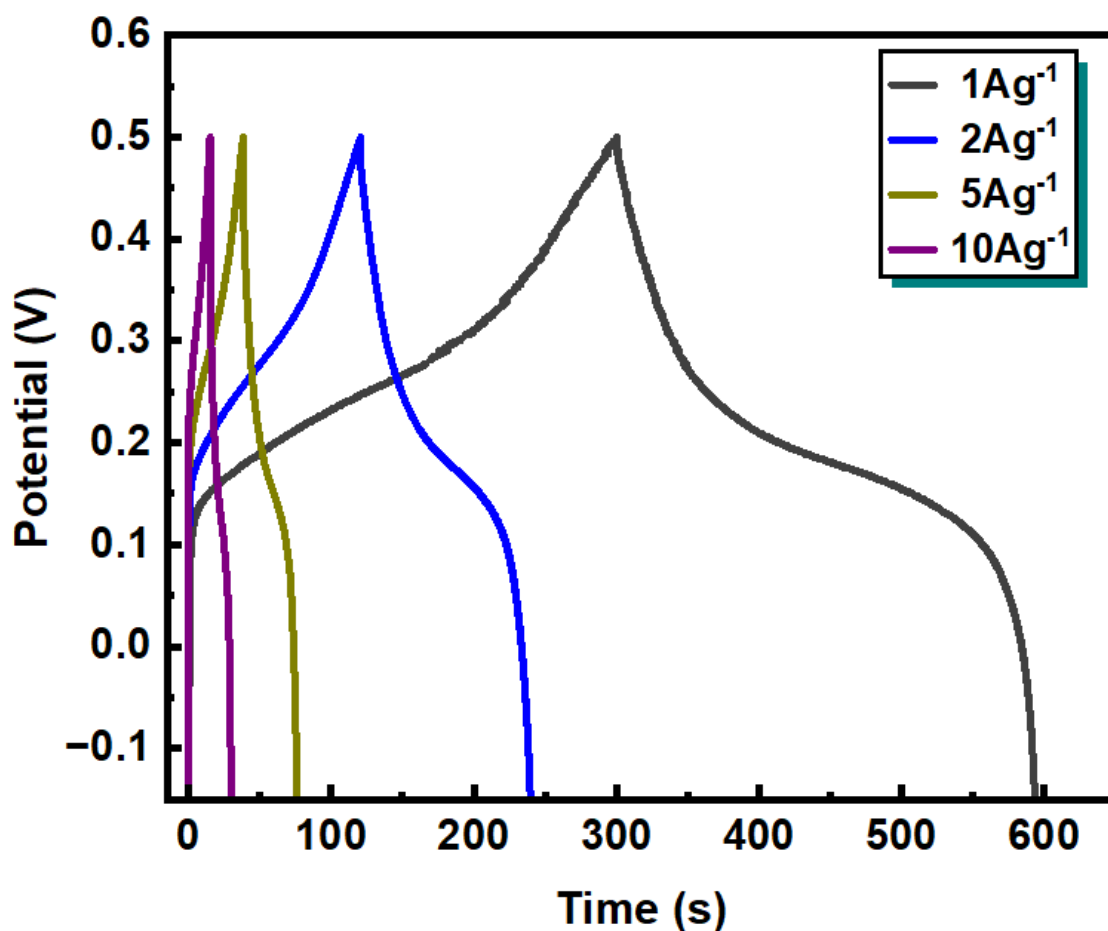


Figure 19: GCD curves for Co@ V₂CT_x (CoV1)

For stability (figure 20), the electrode is subjected to 10000 of charge-discharge cycles and was able to attain a coulombic efficiency of 100% exhibiting excellent cycling stability.

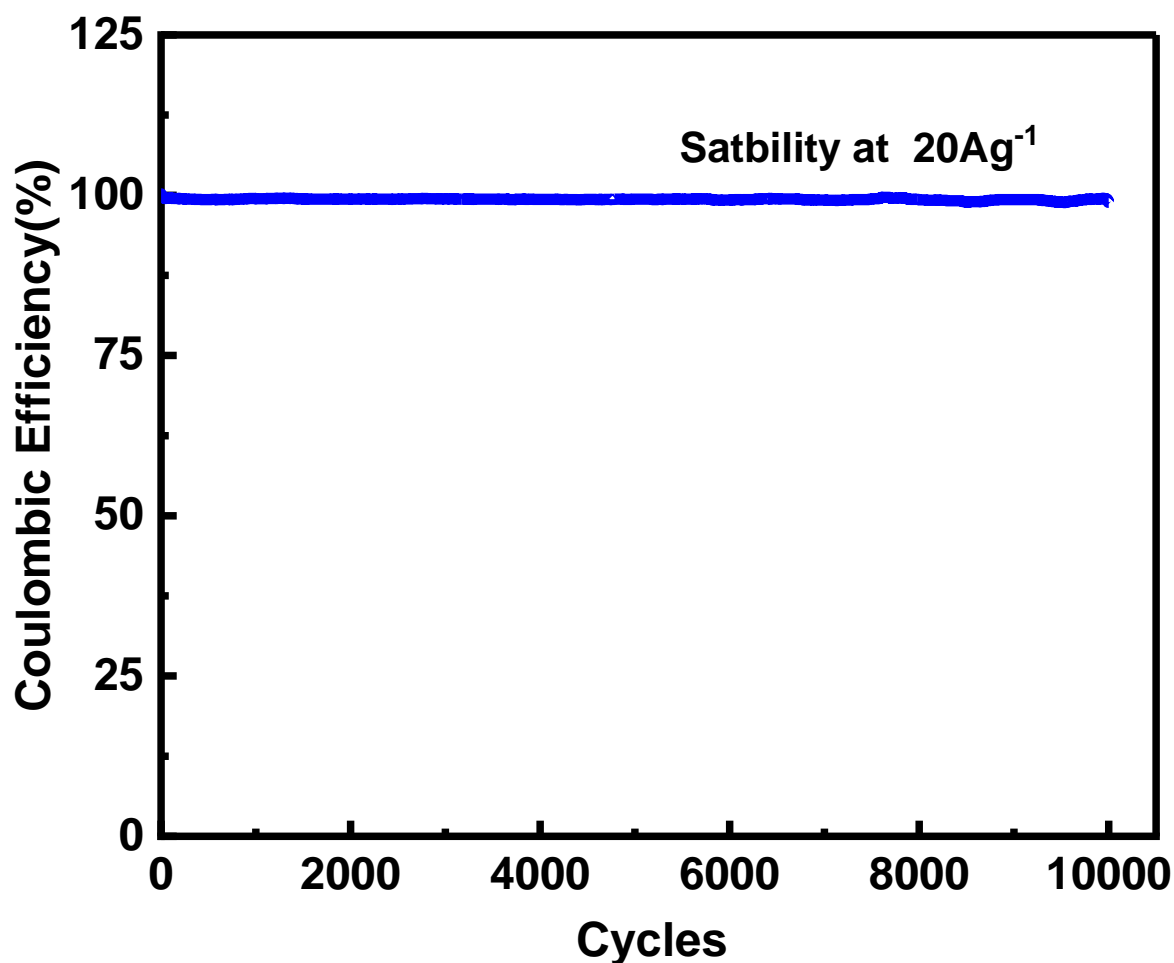


Figure 20: Cycling stability of Co@ V₂CT_x(CoV1)

4.2.3. Linear Sweep voltammetry(LSV)

In LSV, all potentials standardized against reversible hydrogen electrode (RHE) using Nernst equation as $E_{RHE} = E_{Ag/AgCl} + 0.0591pH + 0.205$ and both OER and HER were tested at a constant 10 mVs^{-1} scan rate

4.2.3.1. Hydrogen Evolution Reaction (HER)

V₂CT_x, Co, and Co@V₂CT_x electrocatalysts are assessed in 1.0M KOH electrolyte and at potential of 0 to -1.4V at 10 mVs^{-1} . Figure 21a shows the obtained polarization curves for all samples. The Co@V₂CT_x denoted CoV1(0.5:1), exhibits superior electrocatalytic activity with the minimum overpotential (kinetic barrier) of 103mV at 10 mAcm^{-2} current density, in comparison to V₂CT_x, Co, CoV2 and CoV3 having overpotentials of 293mV, 278mV, 283mV and 201mV respectively (figure 21b).

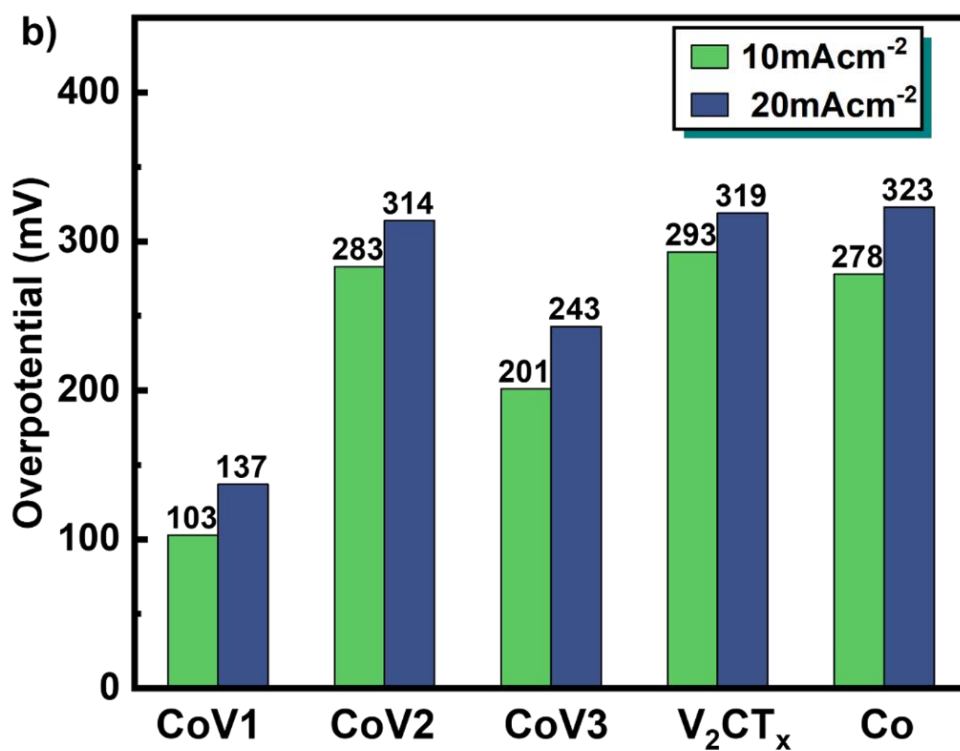
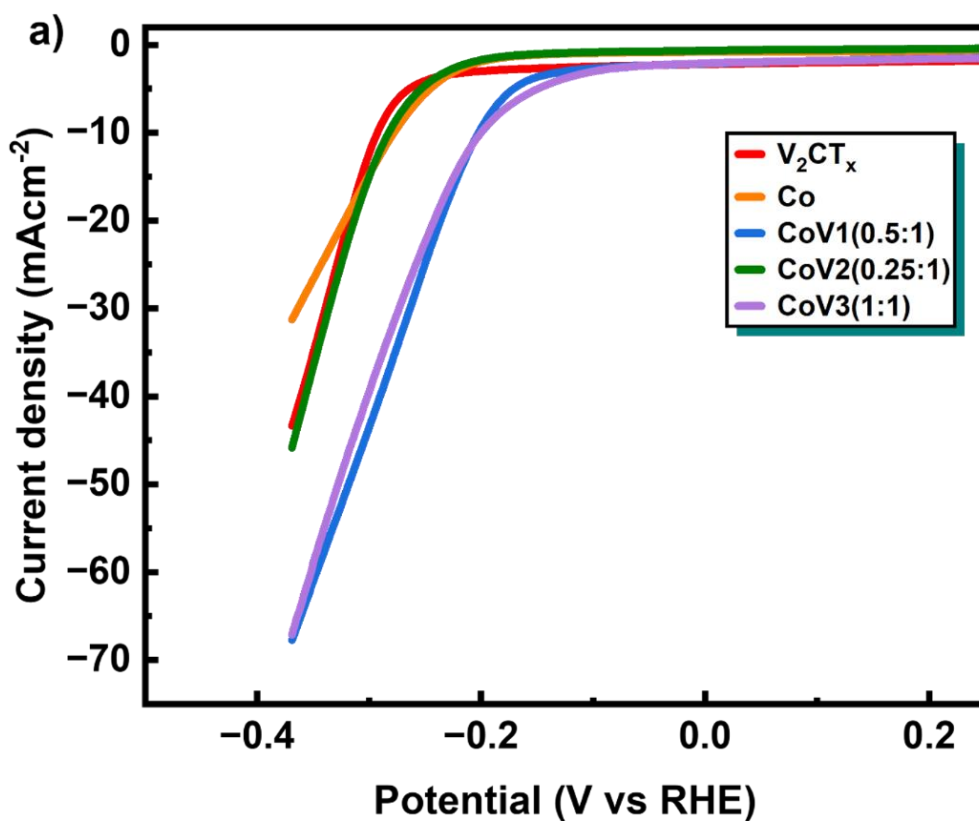


Figure 21: a) HER polarization curves and b) Overpotential at 10mAcm^{-2} and 20mAcm^{-2} for CoV1, CoV2, CoV3, V_2CT_x , and Co

In addition, the CoV1 electrocatalyst recorded at current density of 20mAcm^{-2} , an overpotential of 237mV , which is superior to V_2CT_x (319mV), Co (323mV), CoV2 (314mV) and CoV3 (243mV) (Figure 21 b). This could be because of uniform anchoring of Co on V_2CT_x at best mass ratio of 0.5:1 supported on NF thereby providing the adequate surface area for catalytic activity resulting to a synergistic effect.

The Tafel plots ($\text{Log}|J|$ versus Overpotential) in figure 22 showing Tafel slopes of various samples, was utilized to substantiate the electrocatalytic kinetics. The CoV1(0.5:1) nanocomposites as electrocatalyst shows the least Tafel slope of 83mVdec^{-1} as in comparison to V_2CT_x (110mVdec^{-1}), Co (139mVdec^{-1}), CoV2 (101mVdec^{-1}), CoV3 (136mVdec^{-1}) and commercial Pt/C/NF (81mVdec^{-1}) [36].

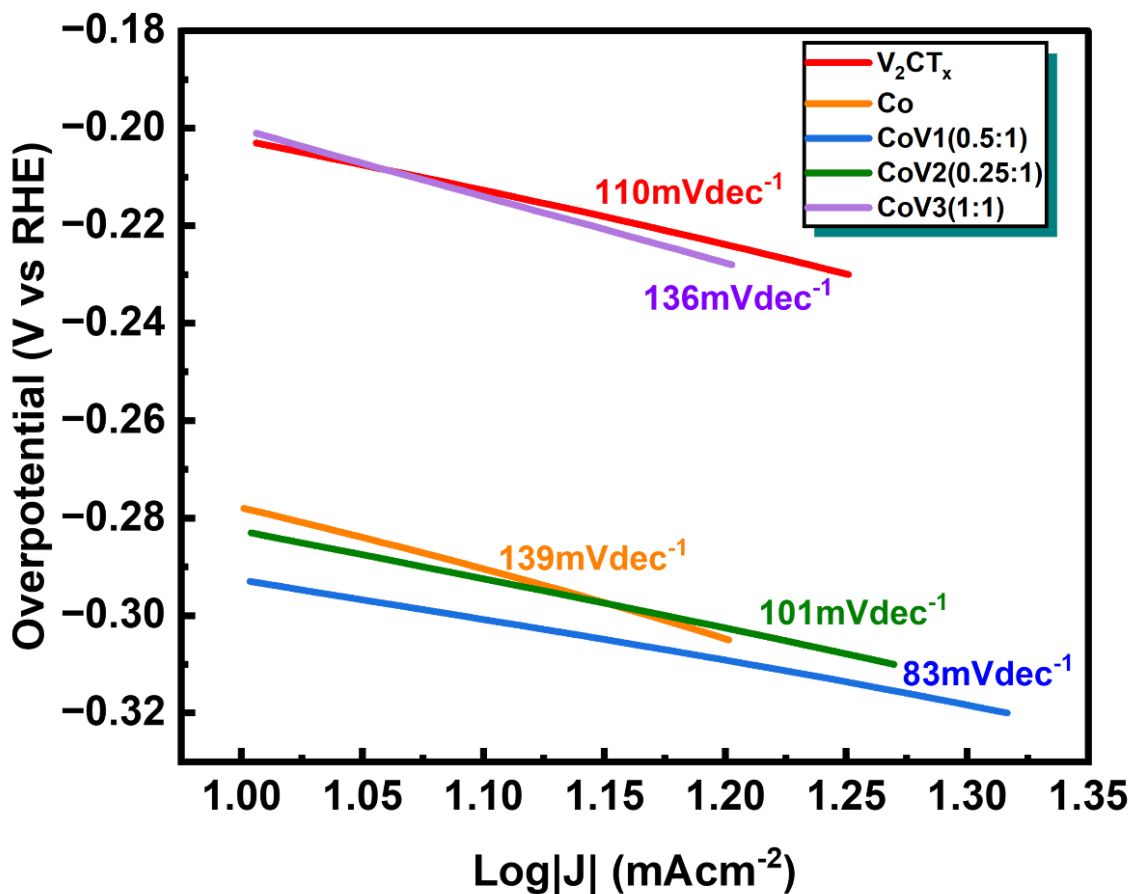


Figure 22: Tafel slope for CoV1, CoV2, CoV3, V_2CT_x , and Co

4.2.3.2. Oxygen Evolution Reaction(OER)

Similarly, to explore the OER , all electrocatalyst were tested in 1M KOH within a set potential of 0 to 0.4V at 10mVs^{-1} .

Figure 23a illustrates the polarization curves of all tested samples. CoV1 exhibits outstanding catalytic activity by producing a minimum overpotential of 170mV at current density of 10mAcm^{-2} as compared to V_2CT_x ,Co , CoV2 and CoV3 having overpotentials of 530mV, 430mV, 400mV and 460mV respectively. At 20mAcm^{-2} , still Cov1 continue to exhibit good catalytic activity with an overpotential of 210mV. The other electrocatalysts- V_2CT_x , Co, CoV2 and CoV3 have an overpotentials of 600mV, 490mV, 450mV and 510 mV respectively at the same current density of 20mAcm^{-2} (see figure 23b).

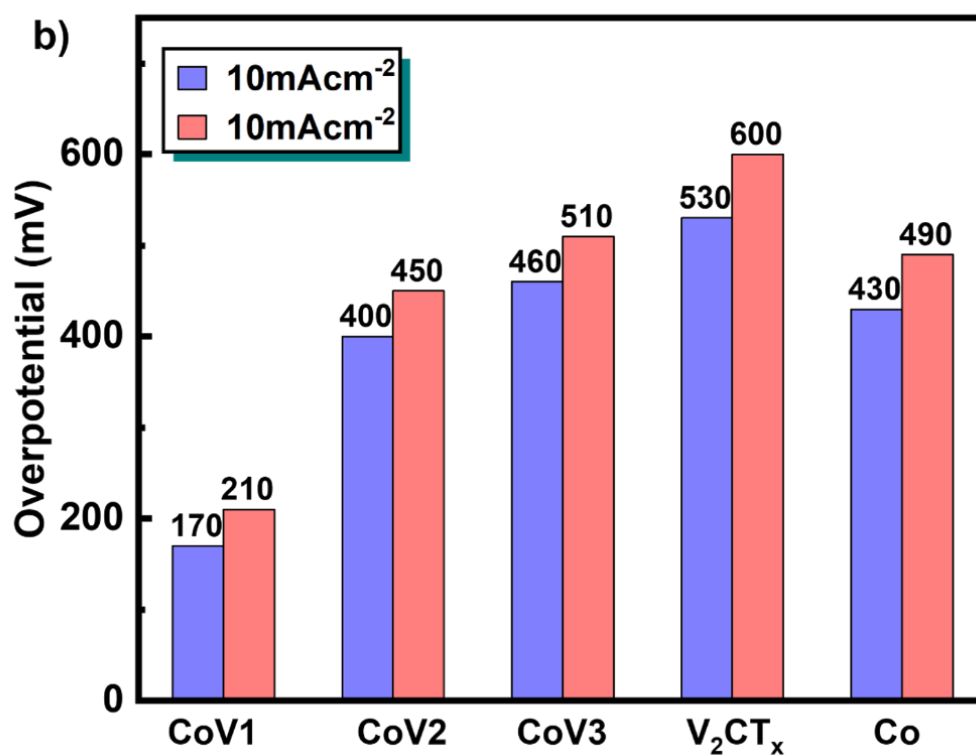
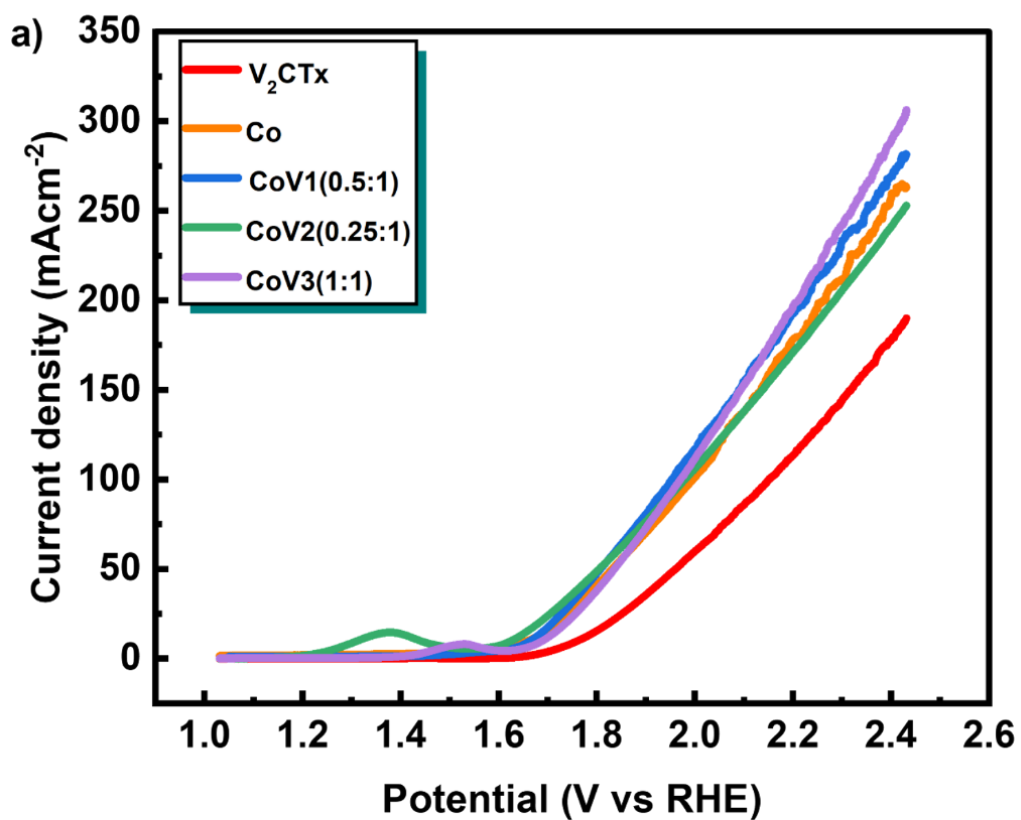


Figure 23: a) OER polarization and b) Overpotential at 10mAcm^{-2} and 20mAcm^{-2} for CoV1, CoV2, CoV3, V_2CT_x , and Co

The Tafel plots ($\text{Log}|J|$ versus Overpotential) in figure 24 showing Tafel slopes of various samples, was utilized to substantiate the electrocatalytic kinetics. The Tafel slope of 145mVdec^{-1} for CoV1 is superior as in comparison to V_2CT_x (207mVdec^{-1}), Co (193mVdec^{-1}), CoV2 (180mVdec^{-1}), CoV3 (156mVdec^{-1}) and commercial RuO_2/NF (67.9mVdec^{-1}) [36].

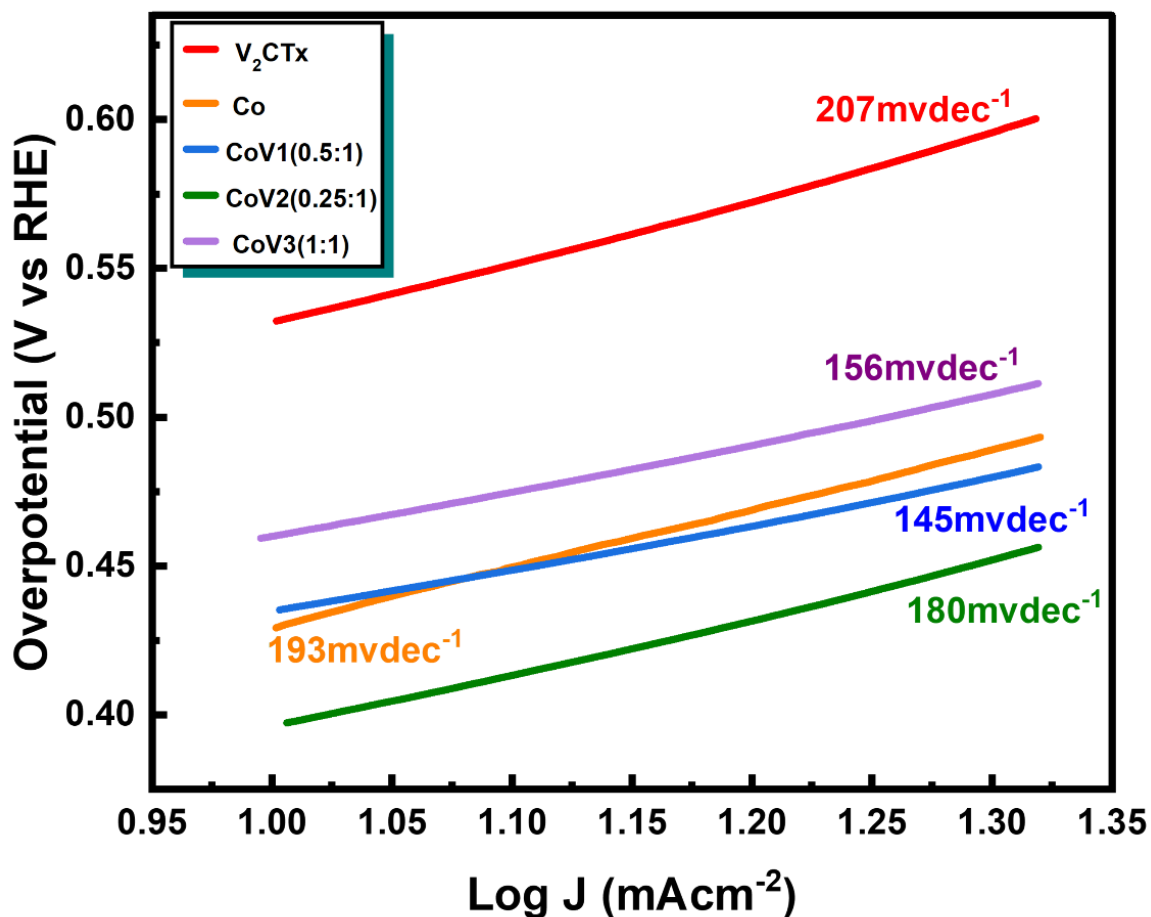


Figure 24: Tafel slopes representing CoV1, CoV2, CoV3, V_2CT_x , and Co.

As shown in Figure 25 below, stability of CoV1 electrocatalyst was tested in 1M KOH and was able to maintain an overpotential of 135mV, at 14.4mAcm^{-2} for 14h hence exhibiting excellent catalytic performance and showed better durability.

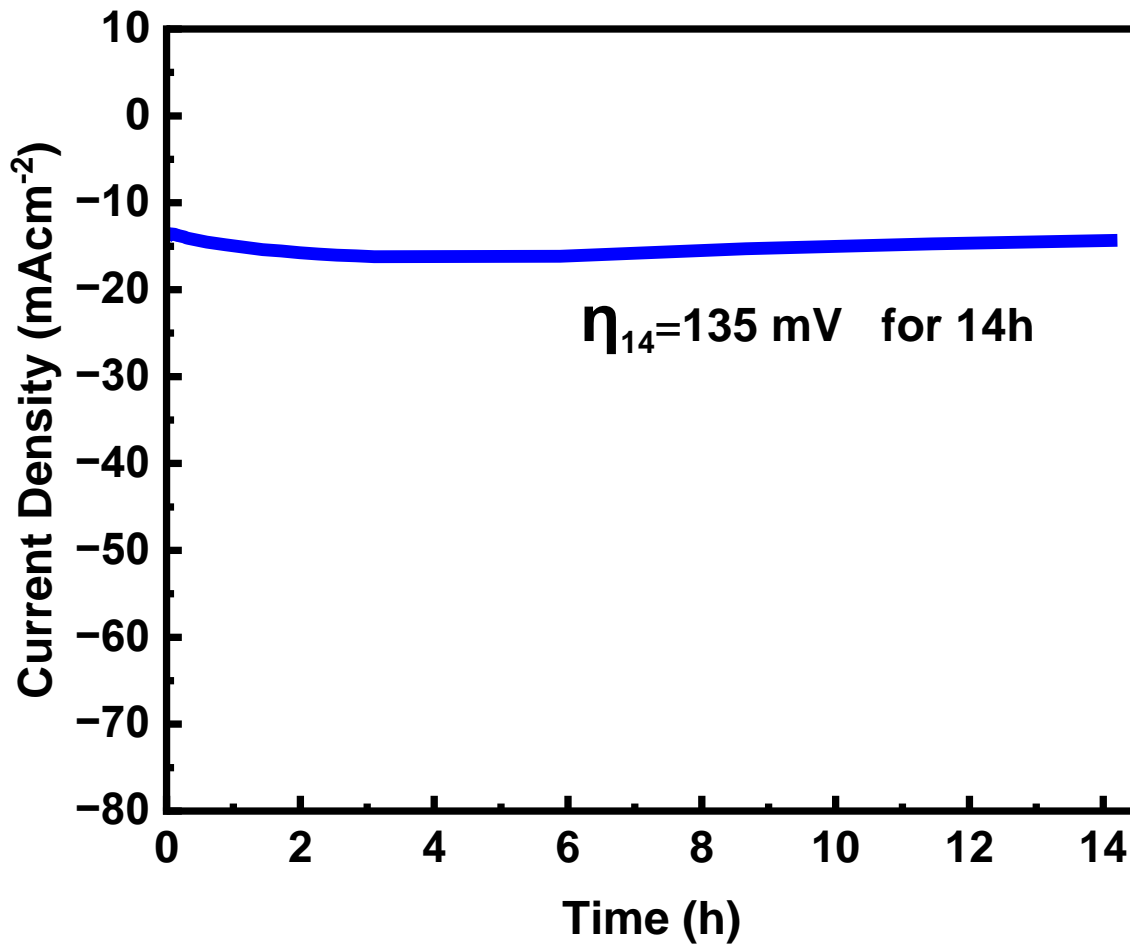


Figure 25: Stability measurements of CoV1 for 14h.

4.2.4. Electrochemical Impedance Spectroscopy (EIS)

EIS was run at a frequency from 20KHz to 0.1 Hz under open circuit potential using a sinusoidal signal of 10mV. All Nyquist plots were best suited with an equivalent circuit to get the resistance of charge transferred.

Figure 26 illustrate the Nyquist plot of V₂CT_x, its fitting and equivalent circuit using Randles model with infinite Warburg impedance. The Catalyst recorded a Charge transfer resistance (R_{ct}) of 224.9 Ω (see table 1).

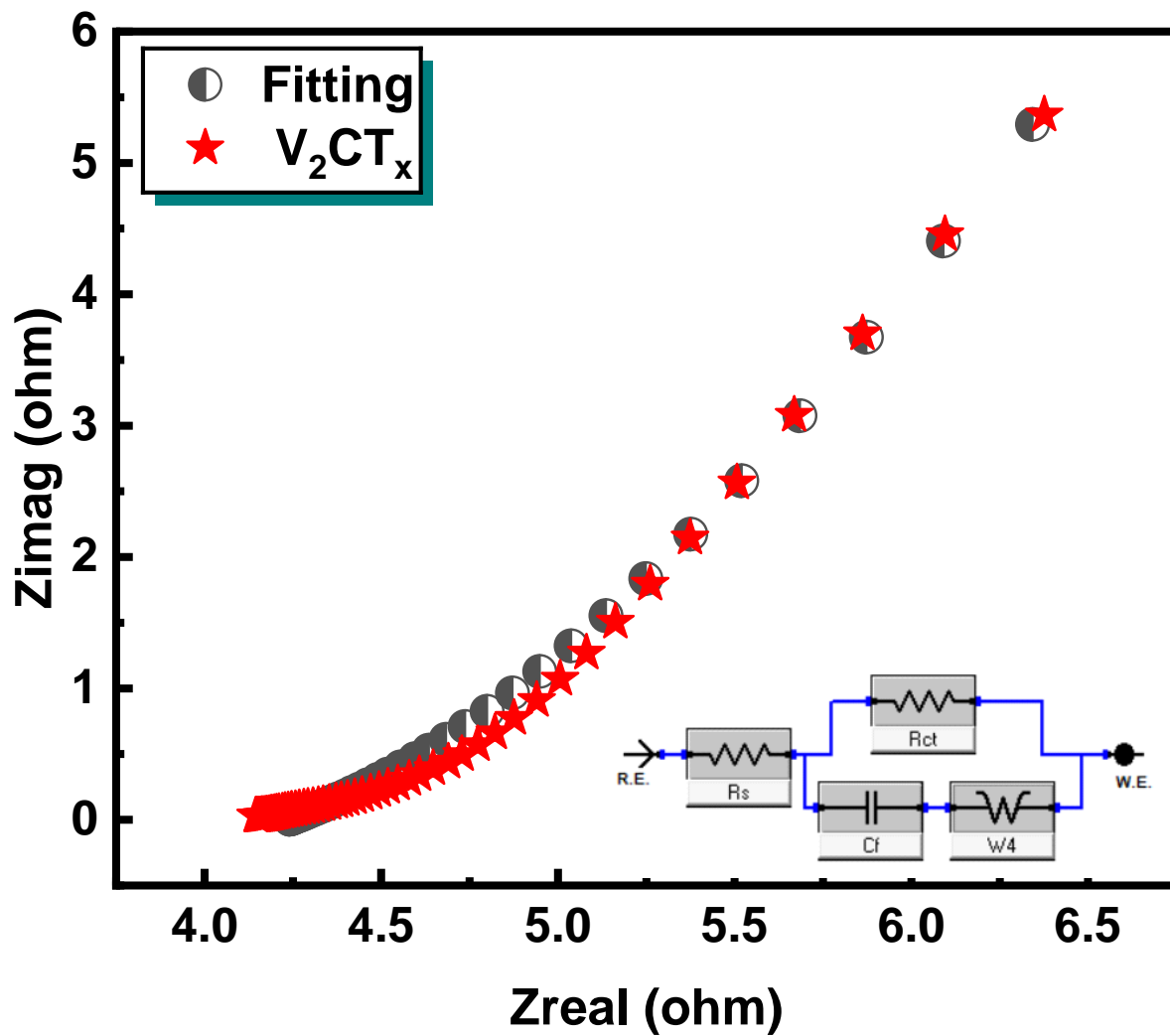


Figure 26: Nyquist plot with fitting and equivalent circuit for V_2CT_x

Moreover, the Nyquist plot of CoV1 sample in figure 27 was fitted with Constant phase element in series to Randles model. The resistance of Charge transferred is just 3.56Ω , signifying good reaction kinetics and rapid transfer of charges.

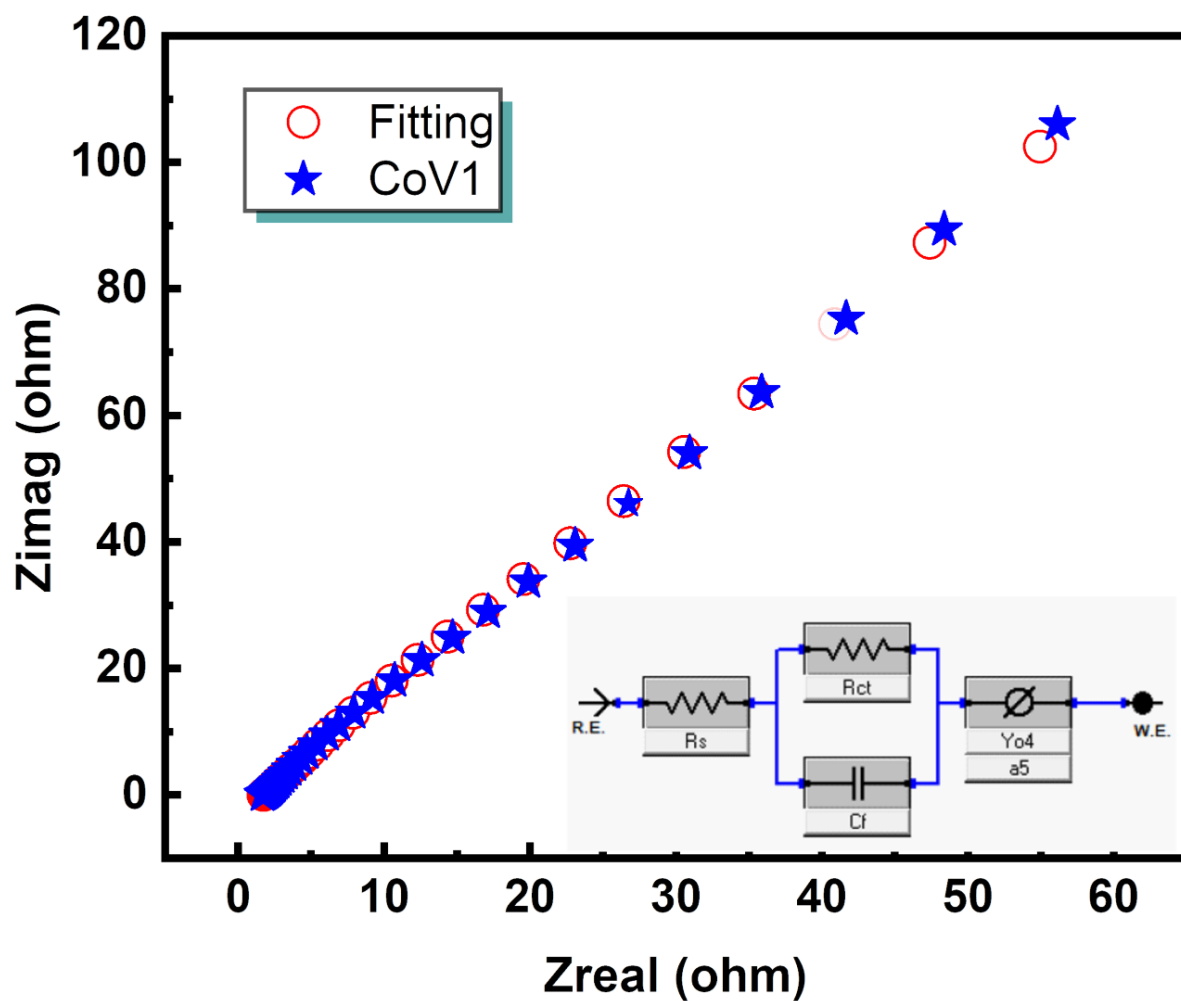


Figure 27: Nyquist plot with fitting and equivalent circuit for CoV1.

	R_s (Ω)	R_{ct} (Ω)	C_{dl} ($mFcm^{-2}$)
Pt/c	4.96	3.43	74.93 [34]
V ₂ CT _x	4.24	224.9	58.9
CoV1	1.74	3.56	97.96

Table 1: Resistant values from Nyquist plots

CHAPTER 5 | CONCLUSION AND WAYFORWARD

This thesis presents synthesis of two-dimensional V_2CT_x MXene via wet-chemical etching using HF. Also, through a one-step simplistic co-precipitation route, Co particles were successfully anchored on V_2CT_x sheets. $Co@V_2CT_x$ of mass ratio 0.5:1 denoted CoV1, stands out to be superior in terms of performance compared to the other nanocomposites. The V_2CT_x provide the conductive surface area and promoted the dispersed growth of Co on its surface, thereby improving reaction kinetics and reduced the obstacle of electron transfer.

As working electrode for supercapacitor, $Co@V_2CT_x$ shows an enhanced performance at $2mVs^{-1}$ scan rate, a gravimetric specific capacitance of $1259Fg^{-1}$. At $1Ag^{-1}$, the $Co@V_2CT_x$ yield a specific charge capacity of $82.2Ahg^{-1}$, energy, and power density of $26.7Whkg^{-1}$ and $325Wkg^{-1}$ respectively. Also, the electrode shows good cycling stability and attained 100% coulombic efficiency after 10000 charge-discharge cycles. Furthermore, the nanocomposite was employed as an electrocatalyst for HER and OER yielding good catalytic activities. For HER, the electrocatalyst provide a small overpotential of 103mV and 237mv at $10mAcm^{-2}$ and $20mAcm^{-2}$ current densities respectively. A minimal Tafel slope of $83mVdec^{-1}$ was achieved which is comparable to commercial Pt/C ($81mVdec^{-1}$). During OER, the electrocatalyst at $10mAcm^{-2}$ and $20mAcm^{-2}$ recorded and overpotential of 170mV and 210mV respectively with a Tafel slope of $145mVdec^{-1}$. The EIS measurements indicated an excellent reaction kinetics with a minimal charge transfer resistance of only $3.56\ \Omega$, comparable to Pt/C ($3.43\ \Omega$). Chronoamperometry test shows that the electrocatalyst can maintain a current density of about $14\ mAcm^{-2}$ for 14hour with only an overpotential of 135mV, thus exhibiting excellent catalytic performance, stability, and showed better durability. The thermogravimetric analysis also confirm that the $Co@V_2CT_x$ nanocomposite is thermal stable up to $1000^{\circ}C$ in air and Nitrogen atmosphere with only 17% weight loss. The remarkable performance of $Co@V_2CT_x$ electrode for supercapacitor and electrocatalyst for water splitting, is as a result of synergetic effects between Cobalt and V_2CT_x MXene together with the surface area and conductive pathways offered by Nickel foam for the movement of ions.

This work provides a simple, easy, and cheap method of preparing MXene composite with nitrate salt. Is also opens door for researchers to explore the many possible applications of MXene composites for both supercapacitors and overall water splitting.

LIST OF PUBLICATION AND SUBMISSION

As of September 28th, 2022, below are the details of papers I have so far.

#	Title / Journal	Authors	status
1.	Zirconia-decoratedV ₂ CT _x MXene electrodes for supercapacitors (Journal of Energy Storage)	Syedah A. Zahra Ebrima Ceesay Syed Rizwan	Published (25 November 2022)
2	Titanium carbide based MXenes for energy storage application (Wiley)	Ebrima Ceesay Shamaila Fatima, Muhammad Z. Iqbal Syed Rizwan ^a	Submitted

REFERENCES

1. Omri, A.J.R. and S.E. Reviews, *An international literature survey on energy-economic growth nexus: Evidence from country-specific studies*. 2014. **38**: p. 951-959.
2. Kraysberg, A. and Y.J.J.o.P.S. Ein-Eli, *Review on Li-air batteries—Opportunities, limitations and perspective*. 2011. **196**(3): p. 886-893.
3. Heubner, C., et al., *Recent Insights into Rate Performance Limitations of Li-ion Batteries*. 2021. **4**(2): p. 268-285.
4. Chu, S. and A.J.n. Majumdar, *Opportunities and challenges for a sustainable energy future*. 2012. **488**(7411): p. 294-303.
5. Pershaanaa, M., et al., *Every bite of Supercap: A brief review on construction and enhancement of supercapacitor*. 2022. **50**: p. 104599.
6. Olabi, A.G., et al., *Supercapacitors as next generation energy storage devices: Properties and applications*. 2022. **248**: p. 123617.
7. Lubitz, W. and W.J.C.r. Tumas, *Hydrogen: an overview*. 2007. **107**(10): p. 3900-3903.
8. Albeladi, n., *A facile method to synthesize bi-functional nanostructured nickel compounds for energy storage and water splitting applications*. 2018.
9. Bossel, U., et al., *The future of the hydrogen economy: bright or bleak?* 2003. **18**(3): p. 29-70.
10. Li, Y., et al., *Recent advances on water-splitting electrocatalysis mediated by noble-metal-based nanostructured materials*. 2020. **10**(11): p. 1903120.
11. Xu, H., et al., *Surface and interface engineering of noble-metal-free electrocatalysts for efficient overall water splitting*. 2020. **418**: p. 213374.
12. Zou, X. and Y.J.C.S.R. Zhang, *Noble metal-free hydrogen evolution catalysts for water splitting*. 2015. **44**(15): p. 5148-5180.
13. Naguib, M., et al., *Two-dimensional nanocrystals produced by exfoliation of Ti₃AlC₂*. 2011. **23**(37): p. 4248-4253.
14. Pang, J., et al., *Applications of 2D MXenes in energy conversion and storage systems*. 2019. **48**(1): p. 72-133.
15. Lukatskaya, M.R., et al., *Ultra-high-rate pseudocapacitive energy storage in two-dimensional transition metal carbides*. 2017. **2**(8): p. 1-6.
16. Mas-Balleste, R., et al., *2D materials: to graphene and beyond*. 2011. **3**(1): p. 20-30.
17. Alhabeab, M., et al., *Guidelines for synthesis and processing of two-dimensional titanium carbide (Ti₃C₂T_x MXene)*. 2017. **29**(18): p. 7633-7644.
18. Tang, X., et al., *MXene-based dendrite-free potassium metal batteries*. 2020. **32**(4): p. 1906739.
19. Zhou, Y., et al., *Ti₃C₂T_x MXene-reduced graphene oxide composite electrodes for stretchable supercapacitors*. 2020. **14**(3): p. 3576-3586.
20. Yun, T., et al., *Electromagnetic shielding of monolayer MXene assemblies*. 2020. **32**(9): p. 1906769.
21. Wu, M., et al., *Ti₃C₂ MXene-based sensors with high selectivity for NH₃ detection at room temperature*. 2019. **4**(10): p. 2763-2770.
22. Wu, X., et al., *Scalable ti₃c₂t x mxene interlayered forward osmosis membranes for enhanced water purification and organic solvent recovery*. 2020. **14**(7): p. 9125-9135.
23. Fan, X., et al., *Plasmonic Ti₃C₂T_x MXene Enables Highly Efficient Photothermal Conversion for Healable and Transparent Wearable Device*. 2019. **13**(7): p. 8124-8134.
24. Libich, J., et al., *Supercapacitors: Properties and applications*. 2018. **17**: p. 224-227.

25. Tian, L., et al., *Advances in noble metal (Ru, Rh, and Ir) doping for boosting water splitting electrocatalysis*. 2021. **9**(23): p. 13459-13470.
26. Chang, H., et al., *Towards high-performance electrocatalysts and photocatalysts: Design and construction of MXenes-based nanocomposites for water splitting*. 2021. **421**: p. 129944.
27. Chen, K., et al., *Vertically pillared V2CTx/Ti3C2Tx flexible films for high-performance supercapacitors*. 2022. **906**: p. 164302.
28. Zahra, S.A., et al., *Enhanced electrochemical performance of vanadium carbide MXene composites for supercapacitors*. 2022. **10**(6): p. 060901.
29. Pan, J., et al., *Designed formation of 2D/2D hierarchical V2CTx MXene/NiV layered double hydroxide heterostructure with boosted electrochemical performance for asymmetric supercapacitors*. 2022. **55**: p. 105415.
30. Fatima, M., et al., *Experimental and computational analysis of mno2@ v2c-mxene for enhanced energy storage*. 2021. **11**(7): p. 1707.
31. Zhang, Y., et al., *Self-assembled Cobalt-doped NiMn-layered double hydroxide (LDH)/V2CTx MXene hybrids for advanced aqueous electrochemical energy storage properties*. 2022. **430**: p. 132992.
32. Sharma, R.K., et al., *Structural Engineering and Carbon Enrichment in V2ctx Mxene: An Approach for Enhanced Supercapacitive Charge Storage*.
33. Park, S., et al., *Reducing the high hydrogen binding strength of vanadium carbide MXene with atomic Pt confinement for high activity toward HER*. 2022. **304**: p. 120989.
34. Zahra, S.A. and S.J.R.a. Rizwan, *MWCNT-modified MXene as cost-effective efficient bifunctional catalyst for overall water splitting*. 2022. **12**(14): p. 8405-8413.
35. Wang, J., et al., *Well-dispersed ultrafine Pt nanoparticles anchored on oxygen-rich surface of V2CTx (MXene) for boosting hydrogen evolution reaction*. 2022. **582**: p. 152481.
36. Yang, L., et al., *FeNi LDH/V2CTx/NF as Self-Supported Bifunctional Electrocatalyst for Highly Effective Overall Water Splitting*. 2022. **12**(15): p. 2640.
37. Pang, S.-Y., et al., *Universal strategy for HF-free facile and rapid synthesis of two-dimensional MXenes as multifunctional energy materials*. 2019. **141**(24): p. 9610-9616.
38. Zhang, W., et al., *Critical Role of Phosphorus in Hollow Structures Cobalt-Based Phosphides as Bifunctional Catalysts for Water Splitting*. 2022. **18**(4): p. 2103561.
39. Xia, L., et al., *Hierarchical 0D– 2D Co/Mo Selenides as Superior Bifunctional Electrocatalysts for Overall Water Splitting*. 2020. **8**: p. 382.
40. Wu, D., et al., *Ultralow Ru Incorporated Amorphous Cobalt-Based Oxides for High-Current-Density Overall Water Splitting in Alkaline and Seawater Media*. 2021. **17**(39): p. 2102777.
41. Zhu, L., et al., *Adjustable antiperovskite cobalt-based nitrides as efficient electrocatalysts for overall water splitting*. 2022.
42. Wu, Y., R. Sun, and J.J.F.i.c. Cen, *Facile synthesis of cobalt oxide as an efficient electrocatalyst for hydrogen evolution reaction*. 2020. **8**: p. 386.
43. Lu, Y., et al., *Anchoring Co3O4 nanoparticles on MXene for efficient electrocatalytic oxygen evolution*. 2020. **65**(6): p. 460-466.
44. Feng, T., et al., *A universal CoO/CoSe2 heterostructure electrocatalyst towards hydrogen evolution reaction via in-situ partial surface-oxidation-selenization method*. 2021. **267**: p. 124644.

45. Ji, X., et al., *Fabrication of hierarchical CoP nanosheet@ microwire arrays via space-confined phosphidation toward high-efficiency water oxidation electrocatalysis under alkaline conditions*. 2018. **10**(17): p. 7941-7945.
46. Prakash, N.J., B.J.J.o.A. Kandasubramanian, and Compounds, *Nanocomposites of MXene for industrial applications*. 2021. **862**: p. 158547.
47. Demazeau, G.J.J.o.M.S., *Solvothermal reactions: an original route for the synthesis of novel materials*. 2008. **43**(7): p. 2104-2114.
48. Cheng, L., et al., *Boosting the photocatalytic activity of CdLa₂S₄ for hydrogen production using Ti₃C₂ MXene as a co-catalyst*. 2020. **267**: p. 118379.
49. Tie, L., et al., *Self-supported nonprecious MXene/Ni₃S₂ electrocatalysts for efficient hydrogen generation in alkaline media*. 2019. **2**(9): p. 6931-6938.
50. Tie, L., et al., *In situ decoration of ZnS nanoparticles with Ti₃C₂ MXene nanosheets for efficient photocatalytic hydrogen evolution*. 2019. **545**: p. 63-70.
51. Hao, N., et al., *In situ hybridization of an MXene/TiO₂/NiFeCo-layered double hydroxide composite for electrochemical and photoelectrochemical oxygen evolution*. 2018. **8**(37): p. 20576-20584.
52. Chen, L., et al., *Quasi zero-dimensional MoS₂ quantum dots decorated 2D Ti₃C₂T_x MXene as advanced electrocatalysts for hydrogen evolution reaction*. 2022. **47**(19): p. 10583-10593.
53. Cruz, I.F., et al., *Multifunctional ferrite nanoparticles: from current trends toward the future*, in *Magnetic nanostructured materials*. 2018, Elsevier. p. 59-116.
54. Zhang, X., et al., *Platinum Nanoparticle-Deposited Ti₃C₂T_x MXene for Hydrogen Evolution Reaction*. 2020. **59**(5): p. 1822-1828.
55. Jian, X., et al., *Three-dimensional carambola-like MXene/polypyrrole composite produced by one-step co-electrodeposition method for electrochemical energy storage*. 2019. **318**: p. 820-827.
56. Rakhi, R.B., et al., *Direct chemical synthesis of MnO₂ nanowhiskers on transition-metal carbide surfaces for supercapacitor applications*. 2016. **8**(29): p. 18806-18814.
57. Tian, W., et al., *Multifunctional nanocomposites with high strength and capacitance using 2D MXene and 1D nanocellulose*. 2019. **31**(41): p. 1902977.
58. Cao, Y., et al., *Enhanced thermal properties of poly (vinylidene fluoride) composites with ultrathin nanosheets of MXene*. 2017. **7**(33): p. 20494-20501.
59. Liang, J., et al., *Heterostructure engineering of Co-doped MoS₂ coupled with Mo₂CT_x MXene for enhanced hydrogen evolution in alkaline media*. 2019. **11**(22): p. 10992-11000.
60. Malaki, M. and R.S.J.A.M. Varma, *Mechanotribological aspects of MXene-reinforced nanocomposites*. 2020. **32**(38): p. 2003154.
61. Gao, L., et al., *MXene/polymer membranes: synthesis, properties, and emerging applications*. 2020. **32**(5): p. 1703-1747.
62. Kumar, S., et al., *Steady microwave absorption behavior of two-dimensional metal carbide MXene and polyaniline composite in X-band*. 2019. **488**: p. 165364.
63. Carey, M., et al., *Nylon-6/Ti₃C₂T_x MXene Nanocomposites Synthesized by in Situ Ring Opening Polymerization of ε-Caprolactam and Their Water Transport Properties*. 2019. **11**(22): p. 20425-20436.
64. Ren, Y., et al., *Synthesis of polyaniline nanoparticles deposited on two-dimensional titanium carbide for high-performance supercapacitors*. 2018. **214**: p. 84-87.

65. Pang, S.Y., et al., *Efficient energy conversion and storage based on robust fluoride-free self-assembled 1D niobium carbide in 3D nanowire network*. 2020. **7**(10): p. 1903680.
66. Sun, Y., et al., *gC₃N₄/Ti₃C₂T_x (MXenes) composite with oxidized surface groups for efficient photocatalytic hydrogen evolution*. 2018. **6**(19): p. 9124-9131.
67. Zhuang, Y., Y. Liu, and X.J.A.S.S. Meng, *Fabrication of TiO₂ nanofibers/MXene Ti₃C₂ nanocomposites for photocatalytic H₂ evolution by electrostatic self-assembly*. 2019. **496**: p. 143647.
68. Cui, B., et al., *Solution-plasma-assisted bimetallic oxide alloy nanoparticles of Pt and Pd embedded within two-dimensional Ti₃C₂T_x nanosheets as highly active electrocatalysts for overall water splitting*. 2018. **10**(28): p. 23858-23873.
69. Kumar, a.a., *development of porous titanasilicate-based hybrid nanocomposites for photocatalytic applications under uv and solar light irradiation*. 2017, national institute of technology warangal.
70. Liu, K., et al., *Raman Spectroscopy: A Novel Technology for Gastric Cancer Diagnosis*. 2022. **10**.
71. Et-Tarhouni, Z., *Engineering mixed surfactant systems to template hierarchical nanoporous materials*. 2015, Cardiff University.
72. Shen, B., et al., *Synthesis of Nb₂C MXene-based 2D layered structure electrode material for high-performance battery-type supercapacitors*. 2022. **413**: p. 140144.
73. Champagne, A., et al., *Electronic and vibrational properties of V₂C-based MXenes: From experiments to first-principles modeling*. 2018. **97**(11): p. 115439.
74. Wu, M., et al., *The synthesis process and thermal stability of V₂C MXene*. 2018. **11**(11): p. 2112.
75. Cao, S., et al., *2D/2D heterojunction of ultrathin MXene/Bi₂WO₆ nanosheets for improved photocatalytic CO₂ reduction*. 2018. **28**(21): p. 1800136.
76. [<https://byjus.com/chemistry/infrared-spectroscopy/>]